JOURNAL OF GEOPHYSICAL RESEARCH, VOL. 112, B06303, doi:10.1029/2006JB004403, 2007

Click Here for Full Article

Rayleigh wave tomography beneath intraplate volcanic ridges in the South Pacific

Dayanthie S. Weeraratne,[1,3] Donald W. Forsyth,[1] Yingjie Yang,[1,4] and Spahr C. Webb[2]

Received 20 March 2006; revised 28 November 2006; accepted 29 January 2007; published 12 June 2007.

[1] We test models for the origin of intraplate volcanic ridges and gravity lineations on young seafloor west of the East Pacific Rise using Rayleigh wave dispersion measured in the Gravity Lineations and Intraplate Melting Petrology and Seismic Expedition (GLIMPSE) seismic experiment. The excellent azimuthal distribution of teleseismic sources recorded over a 12-month period provides resolution of phase velocities at periods up to 100 s. The average phase velocities for the study area reveal a pronounced low-velocity zone reaching a minimum shear velocity of ~3.95 km/s. The negative velocity gradient defining the base of the lithosphere, observed at 40 ± 15 km, abruptly reverses at 70 km depth. The underlying positive gradient changes slope at ~125 km. We attribute these changes in gradient to the onset of incipient partial melting of upwelling mantle in the presence of water at 125 km, followed by increased melt production at 70 km that leads to dehydration of the residual matrix and migration of melt to the surface spreading center. Rayleigh wave tomography shows that there are anomalously low shear velocities extending to at least 50 km depth beneath the Sojourn Ridge and the Hotu Matua volcanic complex, with relatively high velocities between these volcanic chains. These observations are not consistent with passive models for the origin of the volcanic ridges involving lithospheric extension or thermoelastic cracking. Dynamic models invoking flow in the asthenosphere in the form of small-scale convection or viscous fingering instabilities may explain the observed pattern of seismic velocity anomalies.

Citation: Weeraratne, D. S., D. W. Forsyth, Y. Yang, and S. C. Webb (2007), Rayleigh wave tomography beneath intraplate volcanic ridges in the South Pacific, *J. Geophys. Res.*, *112*, B06303, doi:10.1029/2006JB004403.

1. Introduction

[2] Intraplate seamount chains and volcanic ridges are the surface expression of the dynamic interaction between the oceanic asthenosphere and a mobile tectonic plate. One class of these volcanic features seems to be associated with gravity lineations west of the East Pacific Rise (EPR), which are aligned in the direction of Pacific Plate motion in the hot spot coordinate frame [e.g., *Sandwell et al.*, 1995]. We focus on a group of seamount chains and ridges in the South Pacific located on 3–8 My-old seafloor including the well-developed Sojourn Ridge and the actively forming Hotu Matua volcanic complex (Figure 1). These two linear volcanic trends and the Pukapuka Ridge to the south are parallel to plate motion and are spaced about 200 km apart, roughly consistent with the dominant wavelength observed in free-air gravity lineations [e.g., *Haxby and Weissel*, 1986; *Cazenave et al.*, 1992]. Although the formation of seamounts and seamount chains is a direct indicator of the presence of melt in the asthenosphere and its transport through the lithosphere, the origin of the gravity lineations, the mechanism of melt generation, and the relationship of the volcanic activity to the gravity lineations are debated.

[3] The Gravity Lineations and Intraplate Melting Petrology and Seismic Expedition (GLIMPSE) was designed to test competing models for the origin of these volcanic ridges and gravity lineations through petrological and geochemical analyses of dredged basalts, refraction/wide-angle reflection detection of crustal thickness variations, shipboard measurements of gravity, bathymetry and side-scan reflectivity, and probing of upper mantle structure with seismic tomography. The GLIMPSE experiment included the first yearlong deployment of an array of portable, ocean-bottom seismometers (OBS). The long duration of the deployment from November 2001 to December 2002 and the low instrument noise yielded 155 events at distances greater than 2500 km that generated Rayleigh waves with high enough signal-to-noise ratio to be useful for measuring dispersion. The large number of events and the good azimuthal distribution of the sources allow us to (1) test models of the origin of the volcanic ridges by determining the thickness of the oceanic lithosphere and whether anomalously low or high seismic velocities lie beneath the ridges and associated gravity lows; (2) improve constraints on the shape of the low-velocity

[1]Department of Geological Sciences, Brown University, Providence, Rhode Island, USA.
[2]Lamont-Doherty Earth Observatory, Columbia University, Palisades, New York, USA.
[3]Now at Department of Terrestrial Magnetism, Carnegie Institution of Washington, Washington, USA.
[4]Now at Physics, University of Colorado, Colorado, USA.

Copyright 2007 by the American Geophysical Union.
0148-0227/07/2006JB004403$09.00

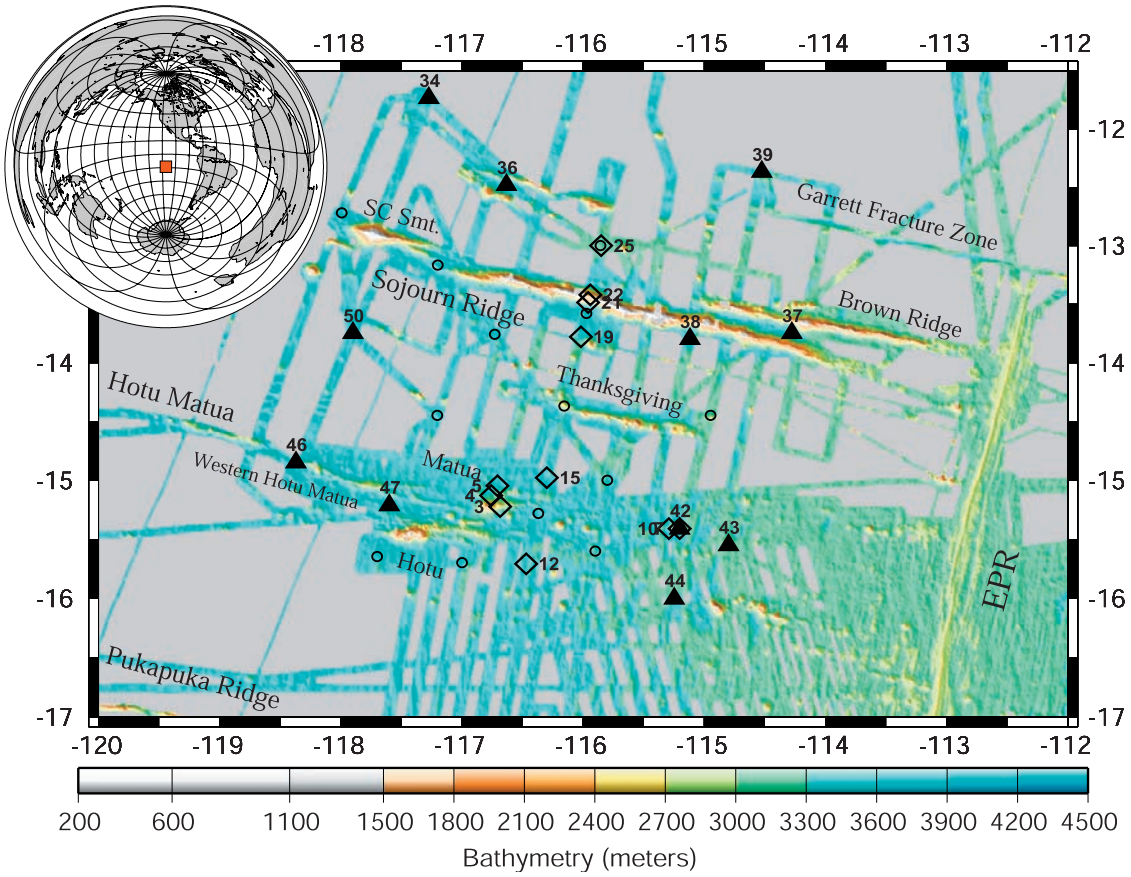

Figure 1. Bathymetry map of the study area, primarily from the GLIMPSE and MELT experiment surveys. The global inset indicates the experiment location in the South Pacific. The Southern Cross seamount (SC smt) was the tallest volcanic seamount we surveyed. The Garrett fracture zone intersects the EPR at about 13.25°S and extends to the west with only subtle relief. OBS deployment sites are shown which recovered data for the refraction and microearthquake studies (open diamonds), long-term deployment (solid triangles), and those which did not return useful data (small open circles).

zone beneath young seafloor; (3) determine the depth extent of seismic anisotropy that is responsible for the shear wave splitting observed in the region [*Wolfe and Solomon*, 1998; *Harmon et al.*, 2004]; (4) measure the attenuation of Rayleigh waves, which will indicate whether melt is required to produce the low velocities in the low-velocity zone (LVZ) or whether they can be produced solely through the effects of temperature, pressure, and water content; and (5) test theoretical predictions that the $\sin 4\theta$ and $\cos 4\theta$ terms, which describe the azimuthal anisotropy of Rayleigh waves (where θ is the azimuth of propagation), should be small in comparison to the 2θ terms [*Smith and Dahlen*, 1973].

2. Models for the Origin of Intraplate Volcanic Ridges and Gravity Lineations

[4] Several dynamic and tectonic models have been put forth to explain the few observations collected from the study of these ocean floor features. The suggestion that mini hot spots are responsible for the chains of ridges and seamounts has been dismissed because the age progression found by dating basalts dredged from the Pukapuka Ridge indicates propagation that is several times faster than Pacific Plate motion [*Sandwell et al.*, 1995; *Janney et al.*, 2000]. If this mechanism were viable, by analogy with observations around Hawaii, we would expect low velocities beneath the leading active end where upwelling and melting are occurring, but little if any velocity changes elsewhere.

[5] Small-scale convective rolls, proposed in early studies to be responsible for creating the gravity lineations [*Haxby and Weissel*, 1986], form as negatively buoyant instabilities dripping from a cooling and thickening lower thermal boundary layer [*Jha et al.*, 1997] or as instabilities within a melt-rich asthenosphere [*Schmeling*, 2000], which are organized into linear rolls by shear in the asthenosphere between the plate and the deeper mantle [*Richter and Parsons*, 1975]. Numerical and laboratory studies have shown that convective instabilities may form beneath seafloor with ages as young as 5 Ma [*Buck and Parmentier*, 1986] although convection at such young ages has been questioned on the basis of laboratory fluid studies [*Davaille and Jaupart*, 1994]. Recent numerical work on convective cooling, however, suggests that convective instabilities may form at young ages but require mantle viscosities as low as 10^{17} Pa s [*Zaranek and Parmentier*, 2004]. Although *Sandwell et al.* [1995] argued that the occurrence of seamount chains or volcanic ridges within the lows of the free-air gravity lineations is inconsistent with a convective origin (Figure 2a), *Harmon et al.* [2006b] have shown that

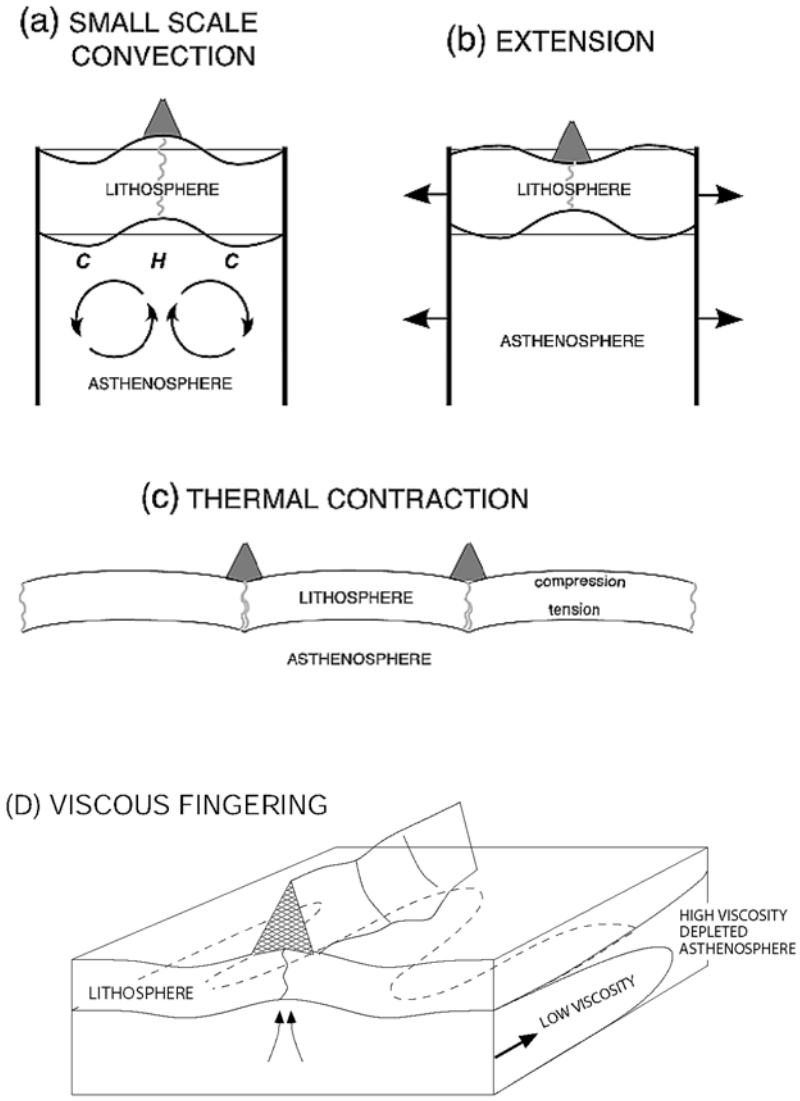

Figure 2. Models to explain formation of seamount chains and gravity lineations in the South Pacific. (a) Small-scale convection [*Haxby and Weissel*, 1986], (b) lithospheric extension and cracking [*Winterer and Sandwell*, 1987], (c) thermoelastic bending and cracking [*Gans et al.*, 2003], (d) viscous fingering instabilities involving anomalously low-viscosity mantle intruded into a higher-viscosity asthenospheric channel [*Weeraratne et al.*, 2003b]. Each model makes unique predictions for lithospheric deformation, asthenospheric flow, and melt generation.

the ridges are actually located on broad topographic highs once the flexure due to the load of the ridge is removed. If melting within the upwelling limb of small-scale convection is responsible for the formation of the ridges, then the higher temperatures should lead to lower seismic velocities beneath the ridges and gravity lows.

[6] Tectonic mechanisms such as lithospheric extension or boudinage (Figure 2b) are expected to allow preexisting melt to percolate up through lithospheric cracks on the seafloor [e.g., *Winterer and Sandwell*, 1987]. If melt exists everywhere beneath young Pacific lithosphere waiting to be tapped by cracks, then the removal of melt to form volcanic ridges should leave anomalously high velocities [e.g., *Karato and Jung*, 1998] beneath the ridges and a widespread low-velocity zone elsewhere. Lithospheric extension should thin the plate, however, creating somewhat lower velocities. Nonetheless, the amount of extension required to produce the gravity lineations is on the order of 10% [*Dunbar and Sandwell*, 1988], which would only produce subtle reductions in velocity and observations of the spacing between fracture zones and has limited the possible extension to far smaller than 10% [*Goodwillie and Parsons*, 1992; *Gans et al.*, 2003]. One of the primary proponents of boudinage has abandoned that model [*Sandwell and Fialko*, 2004] in favor of the suggestion (by *Gans et al.* [2003]) that states that thermoelastic bending stresses produce lithospheric failure in the troughs of plate undulations. This model calls upon a similar melt extraction procedure of tapping preexisting melt in the asthenosphere. In this case, there is a downward deflection of lithosphere and underlying asthenosphere of a few hundred meters expected beneath the ridges but no upwelling of the mantle matrix at all

(Figure 2c), so seismic velocities in the low-velocity zone should be anomalously high where melt has been removed.

[7] A new geodynamic model has recently been proposed that considers viscous fingering instabilities in the asthenosphere, which form when hot, volatile-rich mantle material, such as may be produced from an off-axis mantle plume, travels to the spreading ridge through the asthenosphere [*Weeraratne et al.*, 2003b]. Viscous fingering known as Saffman-Taylor instabilities are found to form at regular wavelengths when a low-viscosity fluid is introduced into a high-viscosity fluid within a Hele-Shaw cell characterized by two closely spaced parallel plates [*Hill*, 1952; *Saffman and Taylor*, 1958]. Viscous fingering is suggested as a model to explain seamount formation in the South Pacific (Figure 2d) as well as a mode of material transport between an off-axis mantle plume (such as the South Pacific superswell region [*McNutt*, 1998; *Montelli et al.*, 2004]) and the spreading ridge system. Higher water content and higher temperatures should cause lower viscosities, lower seismic velocities, and higher melt production as the return flow to the East Pacific Rise ascends under a thinning lithosphere [*Weeraratne et al.*, 2003b]. This model is also consistent with geochemical anomalies or spikes observed along spreading ridge axes associated with nearby hot spot locations [e.g., *Mahoney et al.*, 1994; *Schilling et al.*, 2003]. We suggest that each model discussed above may not be mutually exclusive. For example, compositional or thermal anomalies from viscous fingers could induce upwelling, melting, and small-scale convection.

[8] All of the geodynamic and tectonic models described above require a melt source in the oceanic mantle asthenosphere and point to the need for greater understanding of the low-velocity zone in the oceanic upper mantle. It has long been debated whether the pronounced LVZ in the oceans requires the presence of melt or just the combined effects of temperature and pressure [see recent discussions by *Faul and Jackson*, 2005; *Stixrude and Lithgow-Bertelloni*, 2005]. The observation of reflected or converted shear waves at the base of the oceanic lithosphere [*Revenaugh and Jordan*, 1991; *Gaherty et al.*, 1999; *Collins*, 2003], however, suggests that there must be a sharper transition than expected from increasing temperature alone. The sudden drop in velocity at the base of the high-velocity lid could be caused by a change in seismic anisotropy, the onset of melting, or the presence of water in the asthenosphere, assuming the lithosphere has been depleted of water by melt removal beneath the spreading center [*Hirth and Kohlstedt*, 1996; *Karato and Jung*, 1998]. We contribute to this debate by improving resolution of the shape of the low-velocity zone achieving sensitivity to the base of the LVZ, by providing constraints on the depth distribution of seismic anisotropy, and by measuring seismic attenuation which should be very high in the asthenosphere if high temperatures or high water content are primarily responsible for the low velocities [*Hirth and Kohlstedt*, 1996; *Karato and Jung*, 1998; *Jackson et al.*, 2004].

3. The Marine Seismic Deployment and Rayleigh Wave Sources

[9] The GLIMPSE experiment was conducted in three stages to collect data from a temporary active source, local passive source, and long-term teleseismic deployments. Two microseismic arrays totaling nine OBS were first deployed for a 1-month duration surrounding the Matua seamount and another area of young lava flows east of Matua (Figure 1). A study of these microseismic events is in preparation [*Llenos et al.*, 2003]. The remaining 16 OBS were then deployed for several days in a linear array that crosses the Sojourn and Hotu Matua ridge system to collect active source refraction data [*Holmes et al.*, 2007]. These short-term deployments also recorded teleseismic events used in the surface wave analysis. The refraction OBS were redeployed for the long-term array while the microearthquake sites remained occupied, thus the microearthquake array overlapped the recording period of some of the long-term arrays by as much as 3 weeks. Finally, the microearthquake OBS were recovered and redeployed, resulting in the configuration shown in Figure 1 (triangles and circles), which remained in place for 11 months from December 2001 through November 2002. This long-term array was designed to maximize resolution of vertical and lateral heterogeneities beneath the study area by capturing the highest crossing raypath density of surface waves. The OBS has a short-period (1 Hz) sensor with very high-gain, low-noise amplifiers and provide useful data in the band from 0.005 to 50 Hz [*Webb et al.*, 2001]. Data were also obtained from a few short-period hydrophone records with a useful band above 0.3 Hz. Useful pressure data to periods as long as 40 s were obtained from broadband hydrophone sensors deployed on most of the instruments. All broadband sensors are the Webb design [*Webb et al.*, 2001] amplified sensor with a frequency range from 0.005 to 50 Hz. A few short period hydrophone models were also used in the data set with frequencies above 0.3 Hz.

[10] All OBS's were recovered from the long-term deployment. Only 11 stations, however, produced useful data due to problems with leakage, electronics, and data transfer between the sensor and recording system. The refraction and microseism deployments provided an additional 11 stations that recorded good teleseismic data during the first month. Vertical component data were generally of very high quality, with significantly lower instrument noise than on any of the OBS's in the 1995–1996 MELT Experiment [*MELT Seismic Team*, 1998]. Stations S39 and S50 displayed poor data quality for the first ~40 days before the second automatic releveling was activated [*Webb et al.*, 2001]. During the initial 40 days, we used the broadband hydrophone records of pressure variations in the Rayleigh waves at S39 and S50 to substitute for the vertical component. The hydrophone records yielded good results to periods of about 35 ± 5 s, depending on the amplitude of the signal. S39 stopped recording after 6 months, with no clock calibration available at the end. We estimated the clock drift for S39 from the apparent temporal drift of *P* wave traveltime residuals for 23, well-recorded earthquakes distributed throughout the recording period [*Harmon et al.*, 2006a]. The standard deviation of the estimate of the drift rate corresponds to less than 0.2 s error at the end of the 6-month period. Station S47 provided good data throughout most of the experiment but degraded in quality in the last month before recovery as the battery voltage declined. Station S37 provided good data and timing corrections but no time stamps were recorded

until the instrument was brought onboard, possibly due to a temperature-dependent intermittent connection to the Seascan quartz crystal clock used to prescribe sample frequency. The time stamps for this station, therefore, were back-calculated from the last recorded stamps and rewritten in the binary file before converting to SEGY format, a process that should not introduce timing errors. As part of the Rayleigh wave inversion procedure [*Forsyth and Li*, 2005; *Yang and Forsyth*, 2006a, 2006b], we solve for amplitude corrections at each station to normalize instrument responses. We find that modest, but significant, amplitude corrections are needed at 8 of 22 stations, but these are nearly constant with period and no significant phase corrections are required. At long periods, horizontal components are typically much noisier than the vertical component due to interaction of the ocean-bottom currents with the sensor package causing tilting. The noise level is highly variable from station to station and as a function of time, occasionally approaching the vertical component in quality, but we found no example of better Rayleigh waves on the horizontals than the vertical, so only the vertical component or pressure records were employed in this study.

[11] Despite the loss of data in this pioneering experiment, excellent raypath coverage for Rayleigh wave tomography was obtained due to the ideal location at the center of the Pacific surrounded by earthquake sources on the Pacific rim and the spreading centers of the South Pacific, the long duration of the experiment, the fortunate occurrence of large magnitude earthquakes including seven events that were greater than Ms 7.0, and the reduction in instrument noise due to amplifier redesign [*Webb et al.*, 2001]. We recorded 64 events that yielded useful Rayleigh waves to periods of 50 s and 38 events to periods of 67 s or longer. In contrast, 6 months of recording in the MELT Experiment yielded 12 useful events at 50 s period and only 6 valuable events at a handful of the best stations at 67 s. As demonstrated in the next section, the abundant Rayleigh wave data and the use of new finite frequency tomography methods that improve lateral resolution provide images of heterogeneities at smaller length scales and longer periods than previously achieved by ocean-bottom seismometers.

[12] The excellent azimuthal distribution of 155 events recorded by the experiment at distances greater than 2500 km is shown in Figure 3. Although a total of 22 stations provides data from the different deployments, only a maximum of 11 stations is available for any one event. Several large-magnitude events were recorded from the Aleutian Islands, which added to the high density of earthquakes dominantly originating from North America, South America, and the Western Pacific subduction zones. Earthquakes from southern azimuths were less frequent and smaller in magnitude but provide important azimuthal coverage. The density of crossing raypaths, shown in Figure 4, is greatest for 20–33 s, where more than 140 good events are available (Table 1), and decreases gradually for longer periods. The number of events and seismograms employed at each period is listed in Table 1. Distant events in the northwest Pacific, which have paths passing through deep water, were too scattered to use at periods less than 20 s. Some intermediate depth earthquakes also did not generate useful Rayleigh waves at short periods, so the maximum potential number of 155 events is not obtained for any individual period. Long-period data at 91 and 100 s are limited with only ~15 events large enough to provide good signal-to-noise ratios. There is sufficient crossing path coverage, however, even at the longest periods to obtain a good estimate of the frequency-dependent, average velocity across the study area. The longest periods are essential for providing information about the structure of the LVZ at depths of 100 km or more.

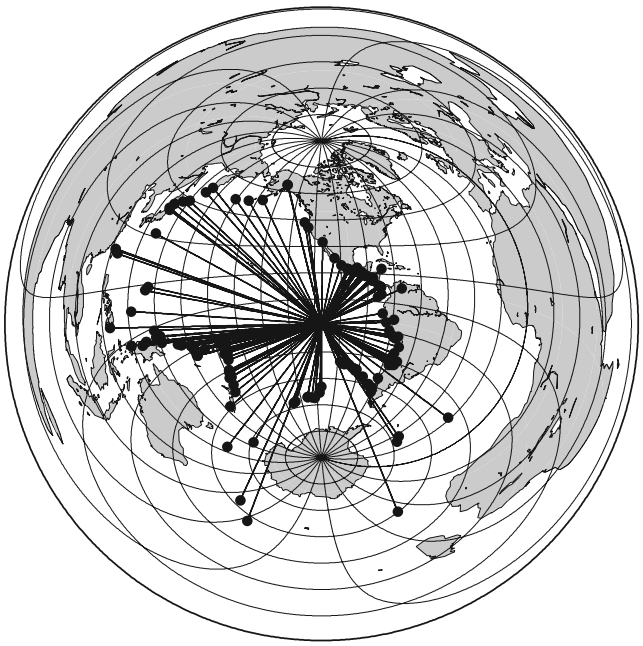

Figure 3. Azimuthal distribution of 155 source events used in this study. Earthquakes (circles) from the Pacific ring surround the study area with ideal distances for Rayleigh wave tomography ranging from 30° to 120°. Nominal ray paths are shown as lines (azimuthal equidistant projection).

4. Surface Wave Inversion

[13] We use a surface wave inversion method that considers scattering effects and deviations from the great circle path caused by velocity anomalies outside the array by representing the incoming wavefield as two interfering plane waves [*Forsyth and Li*, 2005]. This tomographic inversion uses a large number of raypaths that cross both inside the array and outside the station boundaries yielding some control on structure outside the array (Figure 4). At a given frequency, the measured amplitude and phase of the Rayleigh waves at each station, converted to real and imaginary components, are the data. The model parameters include the direction, phase, and amplitude of each of the two plane waves in addition to velocity terms, anisotropy coefficients, attenuation, and station corrections. Statistical averaging of a large number of paths allows improved resolution of vertical and lateral variations in seismic properties such as velocity, anisotropy, as well as attenuation of Rayleigh waves. We solve for the azimuthally

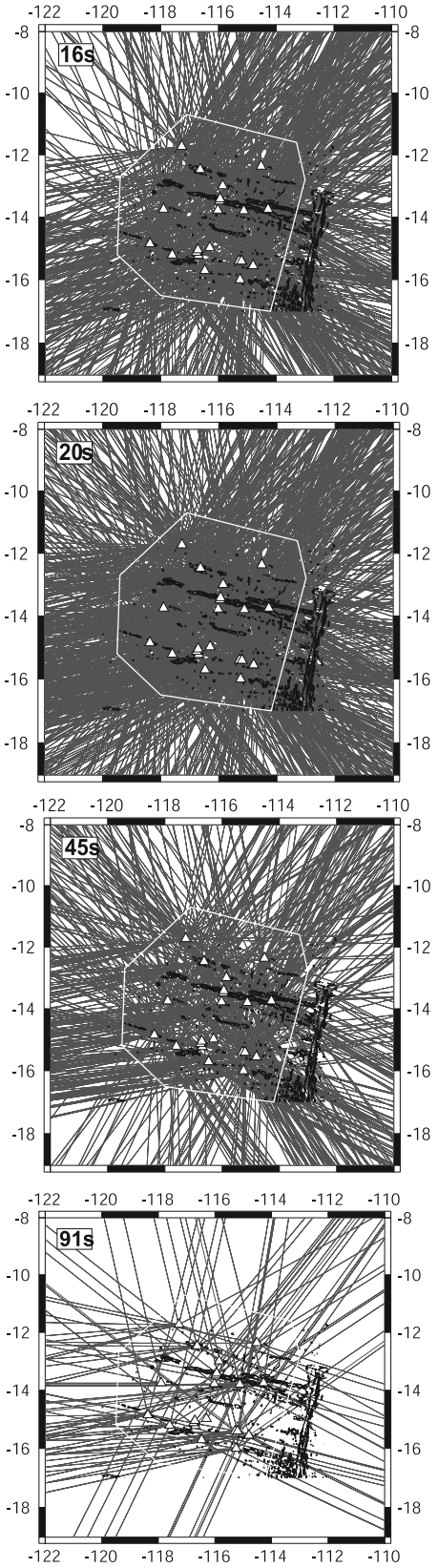

Figure 4. Raypath coverage within our study area (white polygon) recorded at the OBS stations (white triangles) for periods 16–91 s. Event population for each period is also listed in Table 1. Black contours of bathymetry at 500 m intervals from mapped area in Figure 1 are shown for reference.

averaged velocity (B_o), which may vary spatially, as well as anisotropic ($B_i > {}_0$) phase velocities represented by

$$C(\omega,\theta) = B_o(\omega) + B_1(\omega)\cos 2\theta + B_2(\omega)\sin 2\theta + B_3(\omega)\cos 4\theta + B_4(\omega)\sin 4\theta \quad (1)$$

where ω is frequency and θ is azimuth. The last two terms of equation (1) are generally ignored because theory indicates that they should be small for Rayleigh waves [*Smith and Dahlen*, 1973; *Montagner and Nataf*, 1986] and that they are difficult to constrain without unusually good azimuthal coverage [e.g., *Forsyth*, 1975]. Given the ideal azimuthal distribution of seismic events in this study, we take this opportunity to further test this simplification by including the 4θ terms. Attenuation is measured from the diminution in amplitude across the study region. The attenuation effect is too small to observe with individual events but can be reliably found in a simultaneous solution for many events. An initial estimate of average attenuation for an individual period is obtained in a preliminary inversion by simultaneously solving for the best uniform phase velocity, the attenuation coefficient, and the station amplitude corrections. The solutions for these preliminary inversions serve as starting models for subsequent, more complex models.

[14] In this study we improve the representation of phase velocities in the incoming wavefield by incorporating sensitivity kernels that consider finite frequency scattering effects of surface waves [*Yang and Forsyth*, 2006a]. The sensitivity kernels are calculated following the derivation of *Zhou et al.* [2004], which is based on a single-scattering Born approximation, and taking into account the scale of heterogeneities allowed in the model and the frequency averaging inherent in the time windowing applied in our data processing. Sensitivity kernels for each period depend on the smoothing length for lateral velocity variations, phase velocity, period, and the cutting windows used in the data analysis. Examples of the amplitude and phase sensitivity kernels are given in the paper of *Yang and Forsyth* [2006a, 2006b]. Sensitivity is clearly not limited to the great circle path as is assumed in classical tomography techniques. The sensitivity is confined primarily to the first two Fresnel zones; the narrow outer fringes are largely eliminated by interference between the sensitivity of

Table 1. Phase Velocities and Attenuation Coefficients

Period (s)	Events #	Raypaths #	C, km/s	1 Std. Err.	γ, 1/km, $\times 10^{-4}$	1 Std. Err., $\times 10^{-5}$
16	109	1103	3.8158	0.0018	3.40	4.1
18	120	1220	3.8183	0.0019	2.68	3.7
20	144	1461	3.8148	0.0018	2.62	3.4
22	142	1421	3.8144	0.0018	2.67	3.3
25	141	1392	3.8040	0.0019	2.25	3.2
29	130	1282	3.7991	0.0021	2.43	3.1
33	105	1036	3.8030	0.0027	1.58	3.4
40	85	818	3.8039	0.0034	1.75	3.5
45	73	691	3.8150	0.0038	–	–
50	64	602	3.8250	0.0051	1.14	4.1
59	47	448	3.8615	0.0067	1.77	4.9
67	38	349	3.8897	0.0093	0.73	4.8
78	28	259	3.9368	0.0120	–	–
91	16	142	3.9954	0.0200	–	–
100	14	123	3.9882	0.0220	–	–

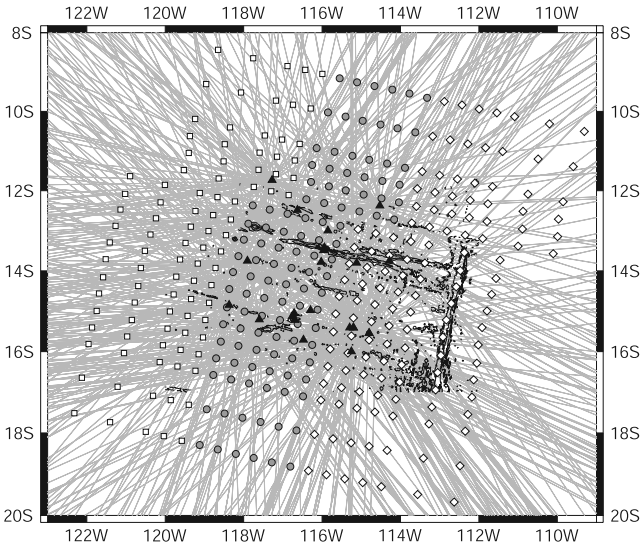

Figure 5. Gridnode locations within the study area where we solve for phase velocity coefficients. The right stepping offset in the grid-node pattern indicates where the Garrett fracture zone produces an offset in lithospheric age. Grid points used for age bins shown in Figure 7 are indicated for 0–4 My (diamonds), 4–8 My (solid circles), and 8–10 My (squares).

different frequencies within the effective pass band and by the Gaussian smoothing described in the next paragraph. In contrast to the Gaussian sensitivity function we employed in previous studies to approximate the effects of finite frequencies [*Forsyth et al.*, 1998; *Li et al.*, 2002, 2003; *Weeraratne et al.*, 2003a, 2003b], this Born approximation approach yields greater sensitivity near the stations, increasing the accuracy and spatial resolution of lateral velocity anomalies. In addition, we also include the amplitude sensitivity function, which further increases the sensitivity to variations in phase velocity by including the amplitude effects of scattering within the array, which were neglected in previous studies.

[15] In the data analysis, we first filter each Rayleigh wave with a 10-mHz-wide band-pass filter with central frequencies ranging from 10 to 60 mHz (16–100 s). We then select data with good signal-to-noise ratio, at least 3 to 1 in amplitude, and window the seismogram to isolate the signal and eliminate avoidable noise. Finally, we estimate the phase and amplitude of the single central frequency, but the time-windowing process implicitly means that we are averaging over a range of frequencies around the central frequency, which is taken into account in calculating the sensitivity function. Inversions are performed separately for each of the 15 central frequencies. Phase velocity coefficients are solved at grid nodes with 50 km spacing in the center of the array and larger spacing along the perimeter well outside the array (Figure 5) although the phase velocity at every point including the grid nodes is a two-dimensional Gaussian weighted average of the coefficients of the neighboring grid points. This averaging effect forces a smooth model on the scale of the 1/e fall-off distance of the weighting function, typically 80 km. The outer grid-node values are essentially undamped and used to "absorb" traveltime variations outside the array, which are not well represented by the two-plane wave approximation. We prescribe a lateral shift in the grid-node pattern north of the Sojourn Ridge where the Garrett fracture zone introduces a right-lateral offset of seafloor isochrons.

5. Rayleigh Wave Phase Velocities

[16] We present the phase velocity data in a multistep process. We first perform a series of inversions for phase velocity, which obtain uniform velocity across the study area at each period. We subsequently consider phase velocities as a function of lithospheric age and two-dimensional variations. Starting models for each successive inversion build on the previous inversion result. As trade-offs between velocity and anisotropy exist, we also solve simultaneously for azimuthal anisotropy in each of these cases. The nearly complete azimuthal distribution of earthquake events, however, significantly reduces this trade-off. We find that there is very little difference in the pattern of two-dimensional variations in velocity between models with and without inclusion of azimuthal anisotropy. Polarization anisotropy from Love wave analysis is not available from this data set due to high noise levels on the horizontal components. In a second set of inversions, we solve for shear wave velocities using phase velocities as the data. Because we have no Love wave data, we are solving for the effective S_V velocity structure rather than the isotropic average S velocity.

[17] The dispersion curve depicting the average or best uniform phase velocity found from an inversion that simultaneously solves for azimuthal anisotropy is shown in Figure 6. From 16 to 20 s, phase velocities are approximately constant at 3.82 km/s. Velocities decrease between 20 and 30 s to a minimum of 3.80 km/s. From 40 to 100 s, phase velocities increase steadily within error to 4.0 km/s at 100 s. Standard deviations are less than 0.002 km/s at short

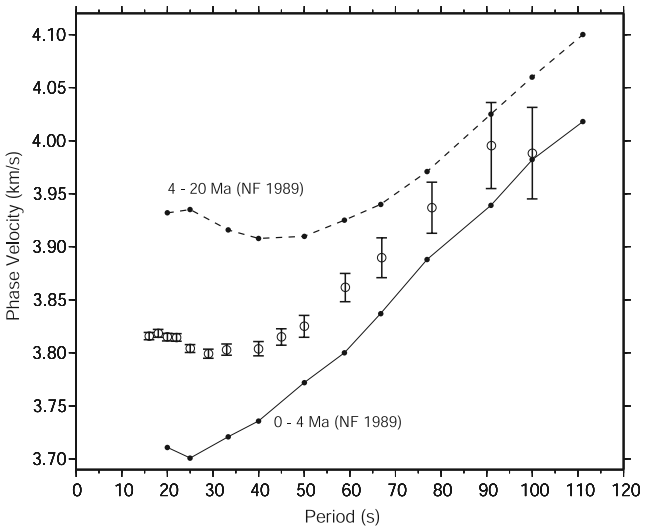

Figure 6. Average phase velocity as a function of period. These results are from an inversion that also solves simultaneously for average anisotropy. Error bars indicate 2 standard deviations. Dispersion curves from previous studies are shown for 0–4 My (solid) and 4–20 My (dashed) [*Nishimura and Forsyth*, 1989].

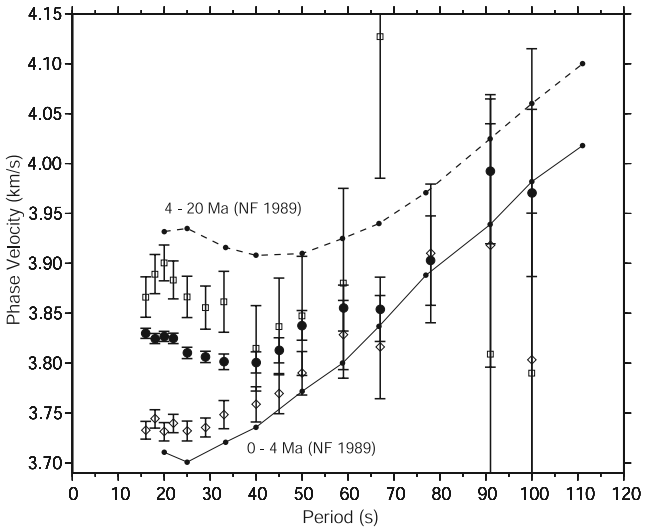

Figure 7. Phase velocity data as a function of period for lithospheric age bins. Symbols for each age bin correspond to Figure 5. Error bars indicate 2 standard deviations. Previous results for seafloor ages 0–4 and 4–20 Ma are shown for comparison [*Nishimura and Forsyth*, 1989].

periods but are larger for long-period data due to increasing wavelengths and reduced data coverage. The phase velocity data from the GLIMPSE experiment (Table 1) for lithosphere with seafloor within the array south of the Garrett fracture zone, ranging from about 3–8 Ma, fall roughly between average dispersion curves for 0–4 and 4–20 Ma (Figure 6) from previous studies of the South Pacific [*Nishimura and Forsyth*, 1989] using land stations. Shear wave velocity inversions will show that the low velocities observed at periods from 20 to 50 s require the existence of an asthenospheric low-velocity zone. The steadily increasing velocities at long periods are the first seismic data from a local experiment indicating sensitivity to the subasthenospheric mantle, as the previous MELT experiment did not provide much data at periods greater than 50 s [*Forsyth et al.*, 1998].

[18] We consider phase velocity variations with seafloor age by breaking up the study area into age bins as shown in Figure 5. Phase velocities for 0–4 Ma (Figure 7) are the lowest, reaching 3.73 km/s at 25 s, and closely follow data from previous studies [*Nishimura and Forsyth*, 1989] although with no stations at the spreading center, our average velocities for this age are probably biased toward the older side. Increasing velocities are observed beginning at 33 s to about 67 s, beyond which fluctuations are evident. Phase velocities are noticeably higher for 4–8 Ma seafloor and fall between the 0- to 4-Ma and 4- to 20-Ma curves from the study of *Nishimura and Forsyth* [1989]. Gradually decreasing velocities between 20 and 33 s are observed, indicating that a low-velocity zone is well resolved below the higher velocity oceanic lithosphere. The increase in velocities at longer periods is less steep and joins velocities for the 0- to 4-Ma age bin at periods greater than 50 s. Velocities for the oldest age bin from 8 to 10 Ma are resolvably higher than the 4- to 8-My dispersion curves. A slight decrease in velocity from 30 to 50 s may be suggested but is not resolved from constant velocity within error. Increasing velocities associated with the subasthenospheric mantle are evident above 50 s.

[19] At periods greater than 50 s, variations with age are not very well resolved. There are several primary reasons. First, the number of paths at long periods is decreased, reducing the lateral resolution. Second, the ability to measure velocity is reduced at longer periods (the same phase error corresponds to greater uncertainty in traveltime.) The Fresnel zone is also wider at longer periods, reducing spatial resolution. Finally, and perhaps most importantly, at longer periods, the waves are most sensitive to structure below the thickening lithosphere. That structure, as we show in this study, is irregular but tends to be aligned perpendicular to the ridge. This nonage-dependent velocity pattern coupled with poorer path coverage that changes somewhat from period to period causes oscillations in Figure 7 at periods greater than 50 s that are somewhat larger than would be expected from the formal error limits. The 4- to 8-Ma age range is entirely within the array and is better constrained than the other age regions, so it contributes most to the average velocities shown in Figure 6. The 4- to 8-Ma phase velocities are within 1 standard error of the average at long periods, but at 100 s, there is the oddity that the best estimates for velocity within all three regions are less than the estimated average velocity. This oddity might seem impossible but actually is due to the fact that the inversions do not solve just for velocity alone but also for wavefield parameters describing the incoming waves from each source. So small trade-offs with the wavefield parameters can make the poorly constrained velocities within age divisions at long periods seem inconsistent with the average, but, considering the standard errors, there is no inconsistency.

[20] Lateral variations in phase velocity that are not constrained to age variations are shown in Figure 8. In our two-dimesional inversions, we use a smoothing length scale of 80 km. In any tomographic inversion, there is a trade-off between spatial resolution and model variance. Tests using a range of length scales show that the model variance increases rapidly when the length scale decreases

Figure 8. Examples of two dimensional phase velocity maps for periods from 16 to 45 s. In the first row, the starting model is the uniform average phase velocity result (shown in Figure 6). The second row uses an iterative two-dimensional starting model described in the text. The third row uses an age-dependent starting model. Standard error contours are shown in the bottom row and are roughly consistent for all models. Phase velocity variations include trade-offs with anisotropy. Gaussian interpolation (smoothing) uses an 80-km length scale. Low velocities are white (red) and high velocities are dark gray (blue) as indicated by the scale bar. The data are masked to show information only in the region considered reliable based on distribution of standard errors shown in plots in the bottom row. White triangles indicate the temporary refraction and microseismic stations which provide events from the first month for periods up to about 50 s. Black triangles are station locations for the long-term deployment. Bathymetry is contoured in black.

below 65 to 80 km, depending on the period. We use 80 km in our final phase velocity models because we want a uniform scale length for all periods, and 80 km provides most of the achievable reductions in data variance. With smaller lengths, the uncertainty in the model velocities and the oscillations in the model increase rapidly without much improvement in fit to the observations. Model damping coefficients in the form of a priori errors (estimated errors assigned prior to the inversion as a starting value) assigned to the starting values of the model parameters can also affect the final velocity anomalies. We use 0.2 km/s as the a priori standard deviation for velocity parameters, which is suffi-

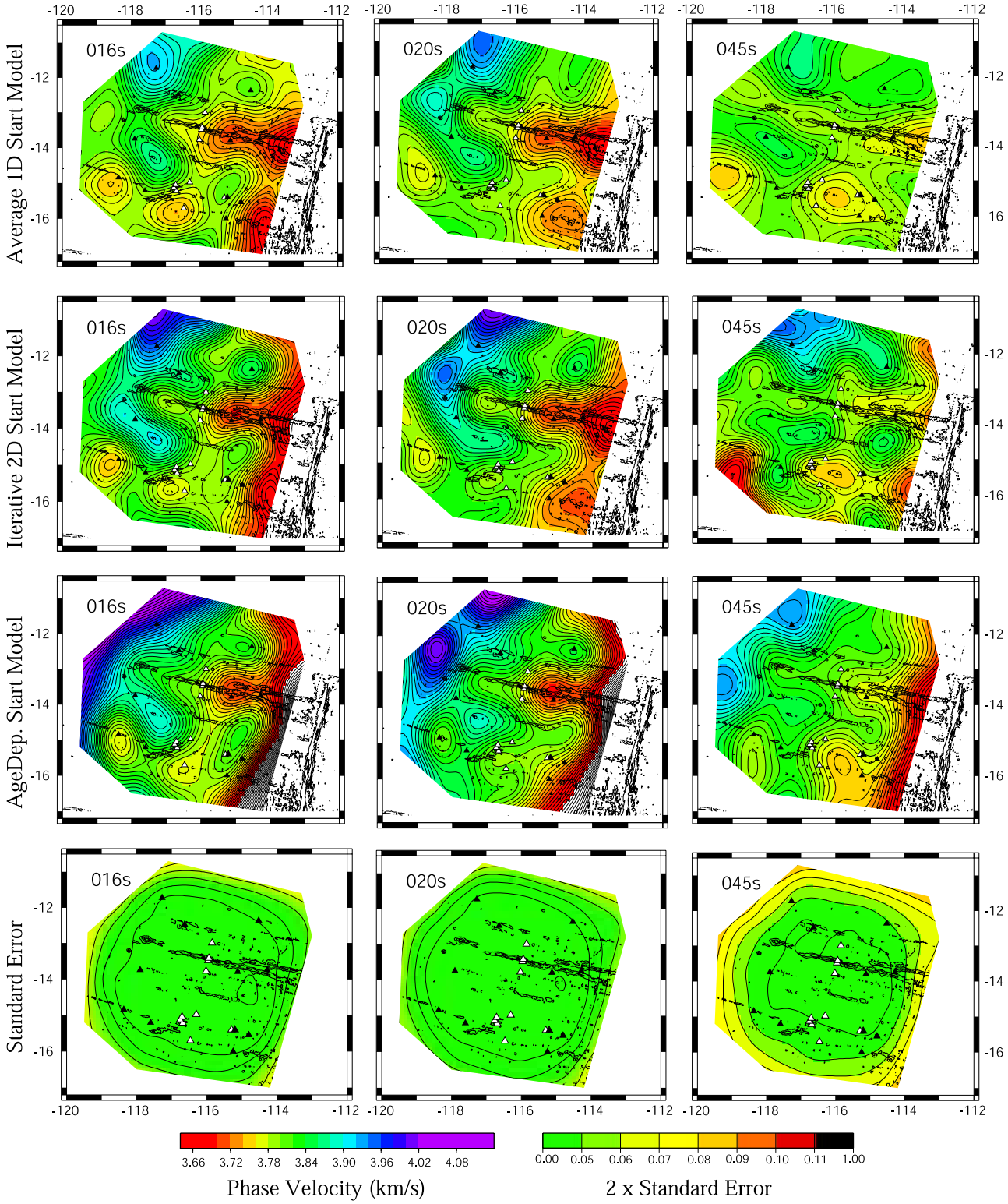

Figure 8

ciently small to stabilize the inversion while having relatively little effect on the final velocity anomalies in areas that have good data coverage.

[21] Our estimates of lateral velocity variations can also be affected by the starting model. We use three different approaches. In the first, we use a uniform starting model at each period with the average phase velocity at each period (Figure 6) assigned to be the starting velocity. Although we iterate to a solution, we retain terms [*Tarantola and Valette*, 1982] that penalize changes relative to the original starting model, not just the change in any one iteration. The resulting phase velocity maps for a few example periods are shown in the first row of Figure 8 for 16, 20, and 45 s. In conjunction with the a posteriori maps (maps generated from the velocity results of the inversion) of standard errors in the velocities (Figure 8, bottom row), this approach provides a simple means of evaluating whether lateral variations at any individual period are significant; if the velocity anomaly at any point exceeds two standard deviations from the mean (starting value), then it is statistically significant at approximately 95% confidence level, or if the difference between two points on the map exceeds two standard deviations, then that difference is significant. At short periods, there are lateral velocity variations of about 0.25 km/s compared to typical standard errors on the order of 0.015 km/s. At these periods, the information provided by the data dominates the inversion, and the a priori information provided by the starting model and its standard deviation has little influence on the final result.

[22] At long periods, however, the model variance is larger, and the velocity variations are smaller. The variations at periods greater than 67 s (not shown), for example, are only weakly significant. In this case, the damping and starting models have a major effect on the result. The uniform starting model is useful for providing a minimum estimate of the required velocity anomalies based independently on phase velocity data at each period, but these maps do not necessarily yield the best estimate of the lateral variations at the longest periods. We know from the results at shorter periods that there are significant variations in structure. Because the kernels at different periods representing phase velocity sensitivity to shear velocity as a function of depth overlap considerably, if one period shows strong lateral variations, an adjacent period should also show the same. Consequently, in our second approach, we use the perturbations at one period added to the average velocity of the adjacent period as the starting model for the adjacent period (Figure 8, second row). We start with the best constrained period of 20 s and apply the perturbations to the starting models for both longer and shorter adjacent periods. We then use the solutions at those periods to generate the starting models at the next adjacent periods, and so on. This is a stable process that does not exaggerate poorly resolved features or map noise into structure because although the sensitivity to structure varies slowly from one period to the next, the noise at each period we have selected is nearly independent (see covariance between periods illustrated in a similar study by *Weeraratne et al.* [2003a]). Because beginning from a laterally varying model relaxes the penalty against changes from a uniform starting model, we also reinvert the 20-s period data using the perturbations from the initial inversion for 20 s as the starting model. At 20 s, this is roughly equivalent to doubling the a priori model variance, reducing the damping, and using a uniform velocity as the starting model. The iterative starting model produces a 1–3% reduction in misfit for periods up to 50 s but is not significantly different from inversions using the uniform starting model at longer periods.

[23] The point to using this stepping, iterative starting model is not to provide a better fit to the data. Both approaches yield models that are acceptable fits to the observations. We look for the dominant features which are observed in both methods that can then can be considered robust. Comparing the phase velocity maps (Figure 8) for the two different strategies for starting models gives an indication of the effects of damping and the robustness of the map features. At short periods, there are few differences, indicating that the starting model and the damping parameter have little effect. At 45 s, we start to see pronounced differences in both the amplitude and the form of the anomalies, with more short-wavelength features present in the models with nonuniform starting velocities. The uniform starting model may lead to an underestimate of the amplitude of velocity anomalies. This is of concern because later, when we invert for shear velocity structure, the absence of anomalies at longer periods, which are sensitive to shear velocities over a greater depth range, may introduce artifacts if the shorter periods require shallow velocity anomalies. The shallow anomalies would also induce some phase velocity anomalies at long periods; if these are overly damped, then the inversion would tend to introduce shear velocity anomalies of opposite sign beneath the shallow anomalies to cancel out the effects of shallow structure on long periods. The nonuniform starting models may tend to exaggerate the persistence of anomalies from short periods to longer periods, but the two approaches should bracket the range of probable variations to allow us to assess whether any reversals of the sign of shear velocity anomalies with increasing depth are required by the data.

[24] We also try a third approach of testing for lateral variations in velocity that differ from an age-dependent seafloor model. Here we first solve for phase velocities as a function of distance from the EPR for each period (using a combined data set from the GLIMPSE and MELT experiments, which provides better coverage of the youngest seafloor in this study). Then we use this age-dependent velocity model as the starting model which solves for two-dimensional variations. The resulting two-dimensional velocity maps are shown in Figure 8 (third row). Slightly lower velocities are observed at younger seafloor east of 114°W near the EPR compared to other model results, and higher velocities are observed in the oldest seafloor west of 116°W. Strong low-velocity anomalies are observed beneath the Sojourn and Hotu Matua volcanic ridges up to 45 s using the age-dependent starting model, as well as in the two previous methods using a uniform one-dimensional starting model (Figure 8, first row) and the iterative starting model (Figure 8, second row), indicating that these features are independent of the starting model and are required by the data. Similarly, high velocities are required between the volcanic chains in all models at periods up to at least 50 s.

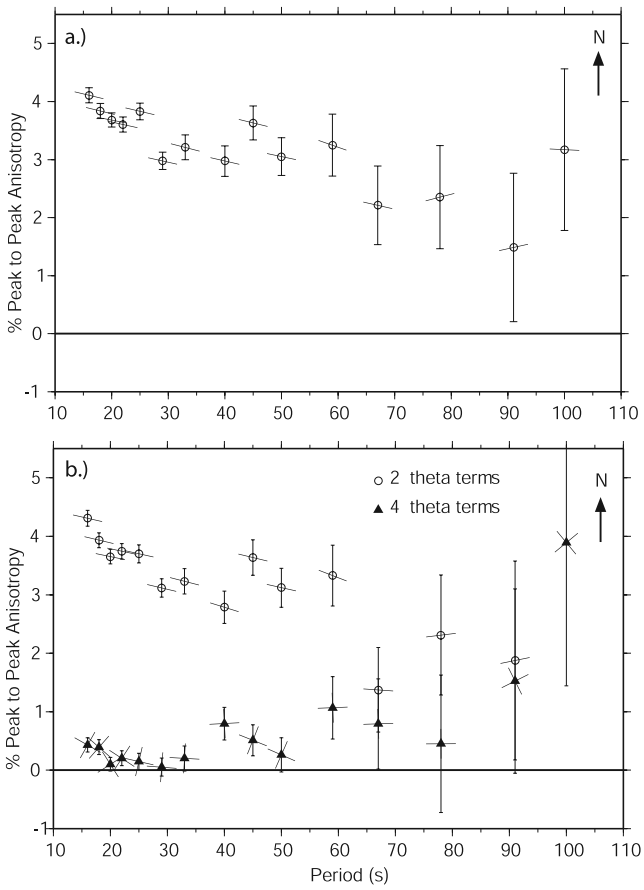

Figure 9. Average anisotropy within the study area as a function of period. (a) Inversion assuming 2θ terms only. Error bars indicate 2 standard deviations. Bars across the symbol indicate the azimuthal direction of anisotropy in map view referenced to the north arrow (top right corner). (b) Anisotropy is shown for 4θ terms (solid triangles) and 2θ terms (open circles). Error bars are ±2 standard deviations. The 4θ terms here have maximum fast directions at 90° intervals.

[25] In all the phase velocity inversions above, we simultaneously solve for average azimuthal anisotropy in the study area. Using only 2θ terms in equation (1), anisotropy is well resolved from zero at all periods (Figure 9a). Peak-to-peak anisotropy averaged over the study area is observed to decrease from 3.9% at short periods, 16–25 s, to 3.3% at longer periods, 29–78 s. Anisotropy may decrease even further to 2.2% at the longest periods above 78 s, but this is not resolved within error. The average fast azimuthal direction for periods up to 67 s is north of 77° ± 2.4°W, consistent with Pacific Plate motion in a hot spot coordinate frame and the fast direction of shear wave splitting [*Harmon et al.*, 2004]. There is some indication of a change in the direction from WNW to WSW-EW for periods longer than 60 s.

[26] Azimuthal anisotropy when the 4θ terms [equation (1)] are included is depicted in Figure 9b. The contribution from 4θ terms, though small, is significant at the 95% confidence level for most periods below 78 s. Neglect of the 4θ terms, however, makes no significant difference in the estimate of the 2θ terms. The 4θ anisotropy of 0.2% at periods up to 33 s increases slightly to 0.7% for longer periods. This increase in 4θ anisotropy appears to coincide with the decrease in anisotropy for 2θ terms at 40 s. The azimuth of anisotropy for 4θ terms shows a change in direction at periods longer than 50 s. Between the two orthogonal choices in direction available for 4θ terms, below 22 s the NW direction is consistent with the direction observed for the 2θ terms. Above 50 s, the direction for the 4θ terms changes to EW, consistent with the change in direction in Figure 9a for 2θ terms at longer periods above 78 s. Though this directional change is not resolved individually for each period in the 2θ terms within error, the consistency with the results from the 4θ terms suggests that this change in direction at long periods may be real.

[27] For the purpose of this paper, we include attenuation as just one of the factors that affects amplitudes. The physical significance of attenuation for upper mantle structure and processes in the GLIMPSE study area is discussed in more detail in another paper [*Yang et al.*, 2007]. Attenuation of Rayleigh waves across the array is measured in a simultaneous inversion for station corrections, lateral velocity variations, and wavefield parameters. The resolution of amplitude variations across a local seismic array is a fairly new achievement for surface wave analysis. The consideration of a large number of raypaths with a dense sampling of the study region offers a statistical advantage over traditional surface wave methods which consider single station-station paths or at best only a few crossing paths [e.g., *Brune and Dorman*, 1963; *Richardson et al.*, 2000; *Saltzer*, 2002]. Scattering or focusing effects in the wavefield are the greatest obstacle to resolving surface wave attenuation.

[28] The two-plane-wave representation of the incoming wavefield provides an approximation of the scattering effects between the source and the receiver array that often explains a large part of the variations in amplitude [*Forsyth and Li*, 2005]. Scattering effects in the vicinity of the array are accounted for with the finite frequency sensitivity kernels, with predicted focusing or defocusing dependent on the local variations in phase velocity. Station amplitude factors at each station correct for erroneous instrument gain and local site responses due to crustal structure. The simultaneous inversion for an attenuation parameter and these other effects on amplitude in combination with a large number of paths allows the reliable determination of Rayleigh wave attenuation in an array with dimensions as small as one to two wavelengths. The decay of energy during wave propagation is described by an exponential, $e^{-\gamma x}$, where γ is the attenuation coefficient and x is the distance. In Figure 10, we show average γ for each period inversion (also see Table 1). The attenuation coefficient decreases with increasing period and is well resolved from zero for periods less than 70 s. Including an attenuation factor yields better resolution of the focusing and wave parameter effects, thus ultimately providing better resolution of the lateral velocity variations through the amplitude sensitivity kernels.

6. Shear Wave Velocity

[29] The average shear wave velocity structure in the study area is obtained from inversion of phase velocity data

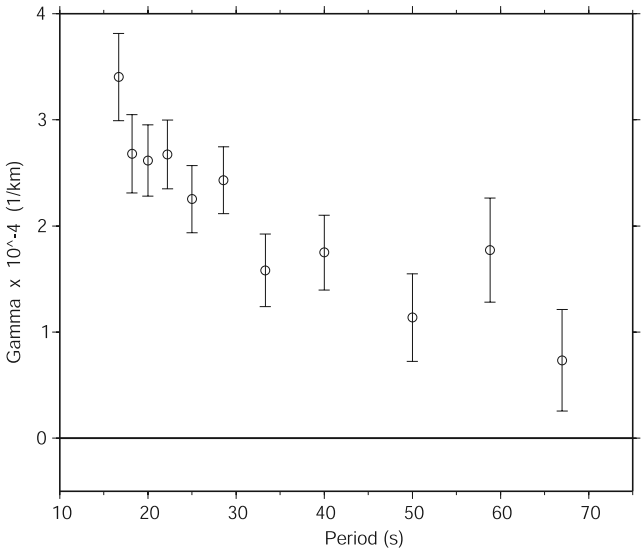

Figure 10. The attenuation coefficient, γ, obtained from uniform velocity inversions as a function of period. No attenuation is expected at $\gamma = 0$. Error bars indicate 2 standard deviations.

for the uniform model (Figure 6). Phase velocities are predicted from a starting shear wave velocity model using partial derivatives calculated from the work of *Saito* [1988]. We use a starting model for 4–20 Ma seafloor [*Nishimura and Forsyth*, 1989] adjusted to account for a 3-km-thick water layer. We use fixed upper and lower crustal shear velocities of 2.6 and 3.6 km/s and *P* velocities of 5.6 and 6.8 km/s, respectively. Densities are fixed as are crustal *P* velocities. In the mantle, we allow for variations in *P* velocity but this has less importance due to the falloff in the effect of *P* velocity for Rayleigh waves with increasing depth. Our models are smoothed by using nonzero terms in the off diagonals of the model covariance matrix forcing some correlations in model changes between immediately adjacent layers. We assign a priori standard deviations of the velocity parameters of 0.2 km/s that provides moderate damping. In our modeling of *S* wave structure, we invert the azimuthally independent phase velocity terms (B_o), for an isotropic model that is effectively the average S_V structure, because we lack S_H information. Although we do not consider the effects of anisotropy directly in the shear wave inversions, but we discuss the possible implications of this neglect for each set of results below.

[30] Shear wave velocities obtained from the average area phase velocity data are shown in Figure 11 and are listed in Table 2. Shear wave velocities are well resolved to ~225 km, below which the starting model strongly influences the data. High velocities of ~4.4 km/s are observed down to approximately 40 km depth associated with the lithosphere. If we define the base of the lithosphere averaged over the study area as the center of the maximum negative velocity gradient [*Weeraratne et al.*, 2003a], we observe a lithospheric depth of approximately 40 ± 15 km.

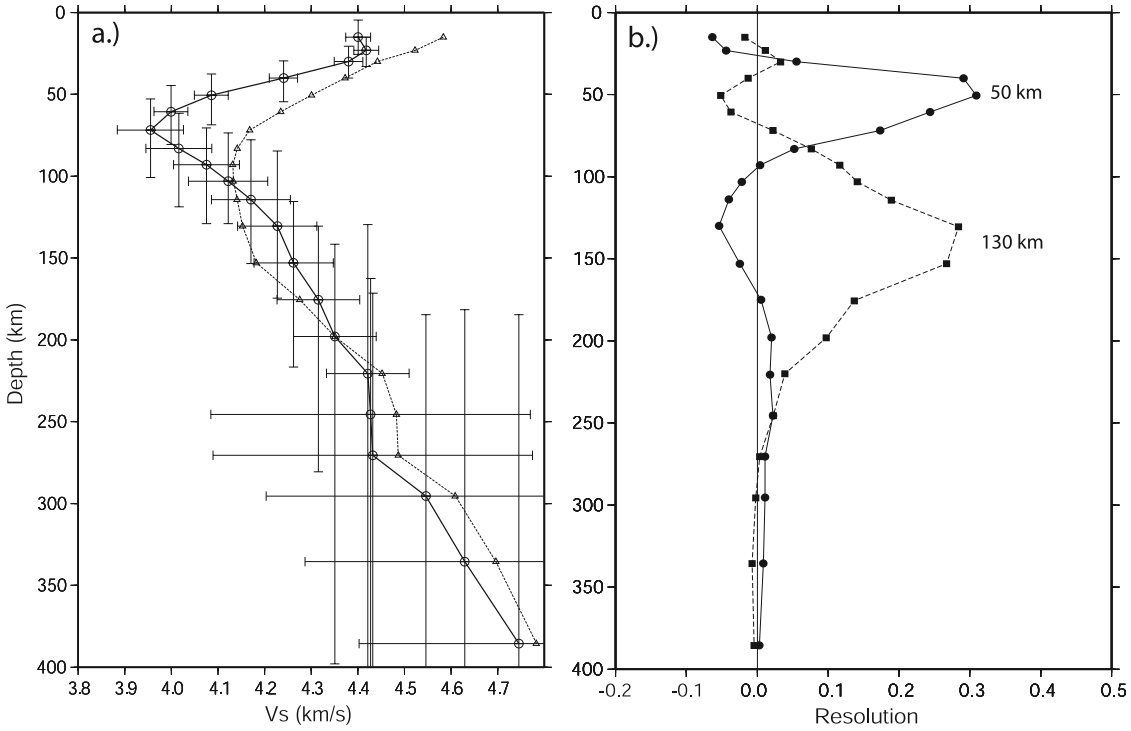

Figure 11. (a) Shear wave velocity as a function of depth from inversion of phase velocity data from Figure 6. The starting model (triangles and dashed line) is 4–20 My shear wave velocity model from previous work [*Nishimura and Forsyth*, 1989]. Vertical error bars represent resolving length at 2 standard deviations (also listed in Table 2). Horizontal bars are 2 standard deviations in velocity averaged over the resolving length, but the model shown is one particular solution, not vertical averages. (b) Resolution kernels for shear wave velocities at 50 and 130 km.

Table 2. Apparent One-Dimensional Shear Wave Velocity

Depth, km	Resolving Range, (−/+) km	V_s, km/s	2 × Std. Err., km/s
15.00	10.5/10.5	4.40	0.03
23.00	8.0/10.0	4.42	0.03
30.00	9.5/10.0	4.38	0.03
40.00	10.5/14.5	4.24	0.03
50.50	13.0/18.0	4.09	0.04
60.50	16.0/20.0	3.99	0.04
71.75	19.0/29.0	3.96	0.07
83.00	21.5/35.6	4.02	0.07
93.00	22.5/36.0	4.08	0.07
103.00	29.5/26.0	4.12	0.08
114.25	36.6/39.0	4.17	0.08
130.50	46.0/44.0	4.23	0.08
153.00	37.5/63.5	4.26	0.08
175.50	45.0/105.0	4.32	0.09
198.00	56.5/200.0	4.35	0.09
220.50	91.0/200.0	4.42	0.09

A negative shear wave velocity gradient extends below this high-velocity lid with shear velocity, β, reaching a minimum of 3.96 km/s at ~70 km depth. From 70 to 130 km depth, shear wave velocities increase sharply to 4.25 km/s, exceeding the velocities of the starting model, and then increase more gradually below 130 km. The positive velocity gradient at the base of the LVZ is independent of the starting model within error and indicates that this steep gradient is required by the data. Examples of the resolution kernel for shear wave velocity centered at 50 and 130 km are shown in Figure 11b. The kernels are reasonably compact, so resolution length, the depth range over which one independent piece of information is resolved, is a useful description. The resolution length increases systematically with increasing depth. The velocities at 50 and 130 km are well resolved over depth intervals of −13/+18 and −46/+44 km, above/below the target depth, respectively. Resolution length and standard errors in average velocity over the resolving length are also depicted by error bars in Figure 11a. The neglect of anisotropy in one-dimensional shear wave inversion may overestimate or underestimate vertical, isotropic velocity heterogeneity if there are significant vertical variations in anisotropy because the azimuthally averaged velocities are also affected by anisotropic structure. Our anisotropy results indicated in Figure 9, however, show a gradual decrease of about 1% from short periods to long periods compared with the ~5% change in average phase velocities (Figure 6) over this period range. We thus conclude that the overall shape of the LVZ in Figure 11 is not significantly affected by changes in anisotropy. If the decrease in azimuthal anisotropy at long periods is caused by a decrease in horizontal alignment of olivine crystals perpendicular to the ridge, then it means that we are somewhat underestimating the isotropic drop in shear velocity from the lithosphere to the asthenosphere.

[31] Lateral variations in shear wave velocity are shown in map view in Figure 12. These maps are constructed from

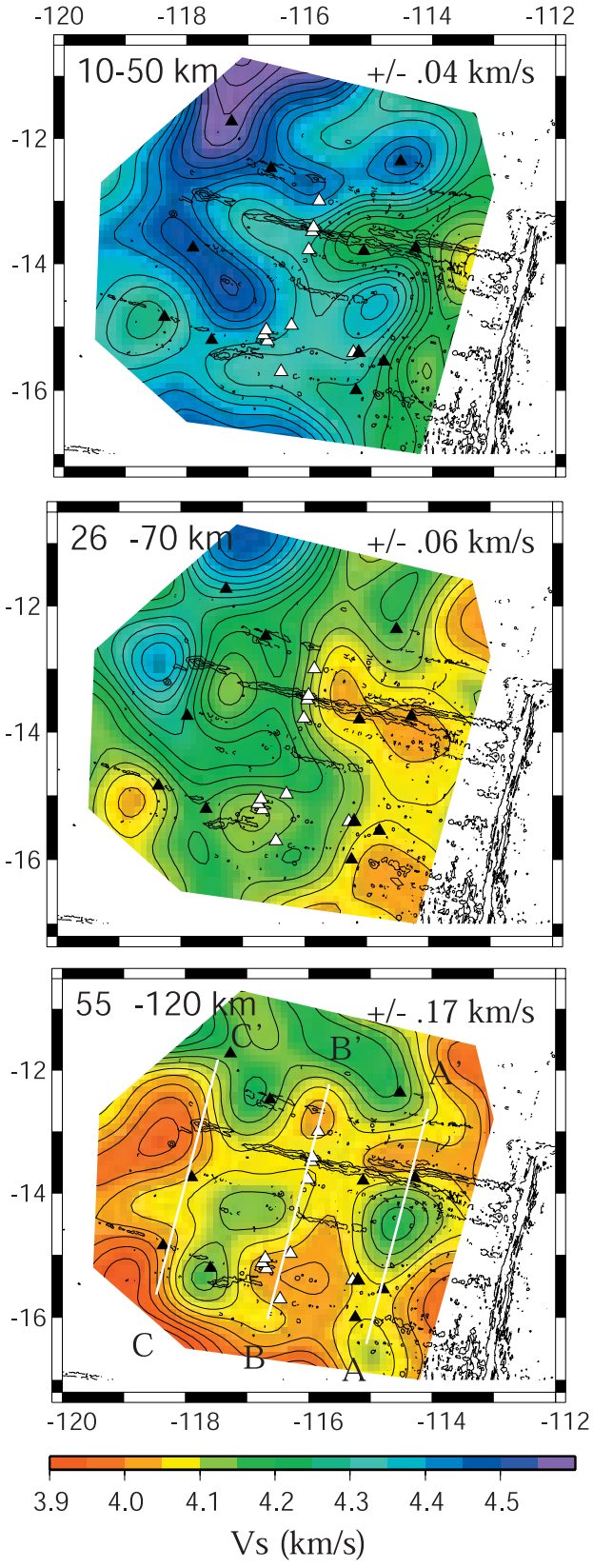

Figure 12. Shear wave velocity maps for depths 10–50, 26–70, and 55–120 km. These maps represent averages over vertical resolving lengths as described in the text. Masked regions are the same as in Figure 8. Contour intervals are 0.03 km/s. The average uncertainty in the mapped areas is shown in the upper right-hand corners (2 standard deviations). Location of seismic stations is shown by triangles. Transects (white lines) are also shown for cross sections A, B, and C in Figure 13.

point-by-point, one-dimensional vertical structure inversions of the two-dimensional phase velocity maps using the average velocity structure (Figure 11) as the starting model. The examples shown are for phase velocities found using non-uniform starting models (Figure 8, second row). To emphasize only those lateral variations that are well resolved, we show in Figure 12 the perturbations averaged over vertical resolving lengths, i.e., 10–50, 26–70, and 55–120 km rather than the poorly resolved variations at individual depths. Note that vertical resolution is poorer for these point-to-point inversions than for inversions of the average velocities. If the degree of anisotropy is laterally constant, these maps of apparent S_V velocity variations will also be a good representation of the isotropic variation in S velocity. Standard errors for 95% confidence limits in velocity averaged over the resolving lengths are roughly constant across the masked study area (indicated in the top right corner); the resolving length itself increases somewhat toward the edges of the map where phase velocities are less well constrained. Lateral velocity variations are largest at shallow depths from 10 to 50 km, where the range of variation is at least 13%. With increasing depth, the range of lateral variations decreases. We note, however, that Rayleigh waves have reduced sensitivity to lateral variations at the longer periods that sample greater depths, which may contribute to the apparent reduction of heterogeneity at these depths.

[32] The most dominant features in the velocity maps are the increase in velocity at shallow depths with increasing age of the seafloor and anomalously low velocities beneath the Sojourn and Hotu Matua seamount chains. Although it is possible that the increase in shear wave velocity with age may be somewhat exaggerated due to a decrease in anisotropy with age [*Harmon et al.*, 2004], the 5–7% changes we observe at depths shallower than 70 km are much larger than the expected anisotropic effect. We divided the study area into regions younger and older than 5 Ma and found no significant difference in azimuthal anisotropy at periods of 30 s or less. There was a significant decrease at longer periods in the older region, suggesting that any age bias would be confined to depths greater than about 50 km.

[33] Anomalously low-velocity regions aligned perpendicular to the spreading center beneath the Sojourn and Hotu Matua trends are as much as 7% lower in velocity than the region between the volcanic chains. These velocity anomalies continue in subdued form into the asthenosphere (55–120 km), but given the larger standard errors, most of the anomalies in this depth range are suggested rather than statistically required. At shallower depths, the low velocities could be interpreted as erosion of the lithosphere beneath areas of recent, off-axis volcanism. The large low-velocity anomaly directly beneath the eastern end of Sojourn Ridge at 10–50 km appears to shift northward beneath the Brown Ridge at greater depths. There also is a suggestion of a weak, low-velocity anomaly parallel to the EPR passing through the center of the Thanksgiving Ridge linking the Sojourn and Hotu Matua trends. High velocities are observed between the two major seamount chains in all maps from 10 to 120 km depth. A 4–6% low-velocity anomaly is persistent beneath the thin line of seamounts west of Hotu Matua down to 120 km. The strong high-velocity anomaly in the NW corner of the study area is persistent to at least 50 km depth and likely reflects the seafloor age offset across the fracture zone. In addition, this area is close to the anti–Bauer scarp where the seafloor increases rapidly in age because much of the spreading was accommodated to the east on the now defunct Galápagos Ridge [*Lonsdale*, 1988; *Goff and Cochran*, 1996].

[34] We also illustrate lateral shear wave velocity variations as a function of depth in cross sections shown parallel to the EPR in Figure 13. High velocities associated with the oceanic lithosphere increase in thickness with increasing seafloor age from A-A′ (near the EPR) at $\sim$20 ± 10 km to C-C′ (farthest from the EPR) at $\sim$40 ± 15 km. The base of the high-velocity lid also demonstrates irregularity, becoming shallower beneath the Sojourn Ridge and Hotu Matua observed most strongly in A-A′ and B-B′. Anomalously low velocities are observed at mantle depths between 50 and 80 km beneath the Sojourn Ridge and Hotu Matua, associated with the asthenosphere, but are absent in the region between the volcanic ridges at these depths. The color scheme we employ highlights changes in the shape and depth of the LVZ minimum, but many of the changes at sublithospheric depths are only suggested by the data and fall below the level of confident resolution in this cross-sectional profile.

7. The Oceanic Asthenosphere

[35] The Rayleigh wave dispersion data from the GLIMPSE Experiment described in this paper (Figure 6) provide the first real control on the shape of the low-velocity zone beneath young oceanic lithosphere from a local seismic array. The MELT Experimental data did not extend to long enough period to resolve the bottom of the low-velocity zone but instead relied on a combination of local, short-period observations and dispersion over teleseismic distances from previous studies [*Forsyth et al.*, 1998]. The positive velocity gradient above about 125 km is significantly steeper than the gradient at greater depths (Figure 11). We interpret the change at 125 km as being caused by the onset of a small degree of partial melting in the presence of water. The melt fraction is probably very small and may not segregate from the matrix. Abruptly at a depth of about 70 km, the velocity gradient reverses, with shear velocities increasing rapidly toward the surface. This sharp reversal of the velocity gradient at 70 km may be caused by an increase in the rate of melting of the rising mantle beneath the ridge at this depth as predicted by petrological models, extraction of the melt by migration toward the surface, and the consequent dehydration of the residual matrix. The dehydration effect apparently overwhelms the effect of any remaining melt above 60 to 70 km in controlling the gradient although the low velocities may still require the presence of some melt, particularly beneath the volcanic ridges, as described in the next section.

[36] We appeal for dehydration instead of cooling of the uppermost mantle for the gradient reversal because 70 km is much deeper than the expected vertical extent of conductive cooling of the lithosphere within the first few million years. The conclusion that dehydration plays an important role is strongly supported by the observation of a rapid increase in anisotropic electrical conductivity at depths greater than about 60 km (beneath the eastern side of the East Pacific Rise) [*Evans et al.*, 2005], indicating an increase in water content, and by the attenuation structure, which is incom-

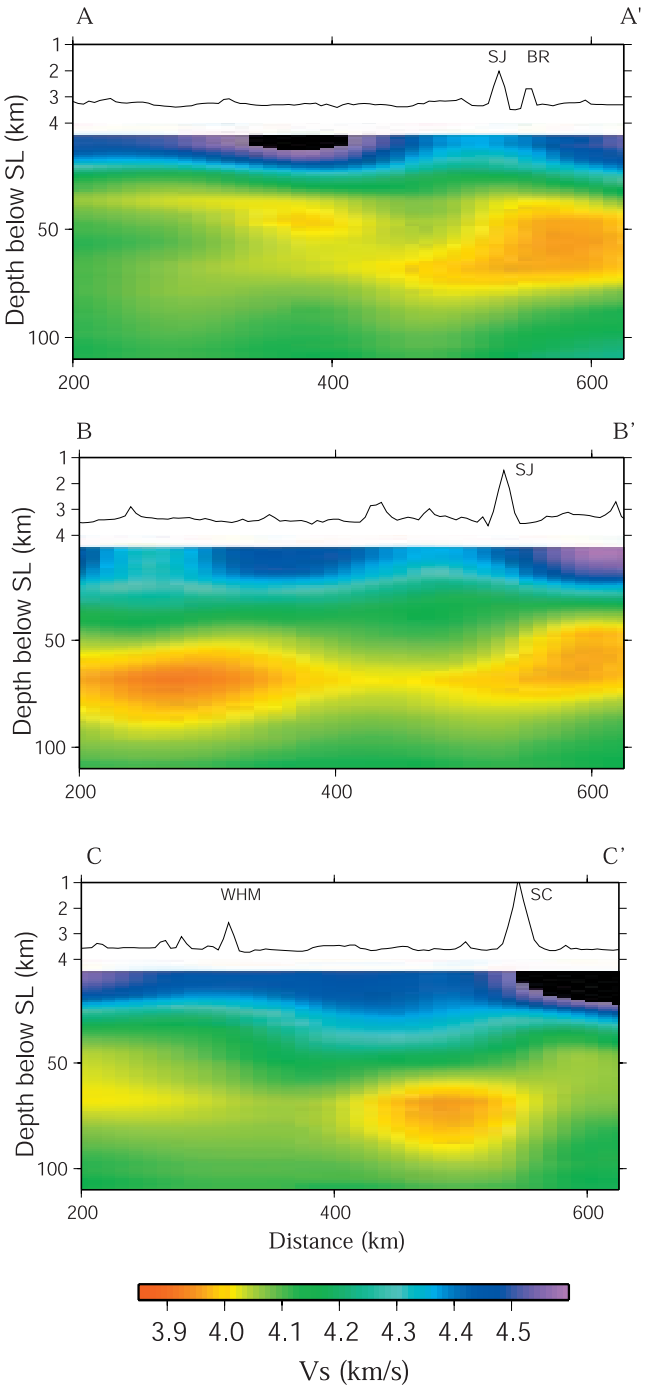

Figure 13. Shear wave velocity cross sections parallel to the East Pacific Rise. Locations are shown in Figure 12. Velocity contours are drawn at 0.03 km/s intervals (color version of Figure 13 shows color gradations at 0.01 km/s). The depth scale from 1 to 4 km is stretched to show the exaggerated bathymetry along each transect. Abbreviations for bathymetric features are labeled as Sojourn Ridge (SJ), Southern Cross seamount (SC), western Hotu Matua (WHM), Thanksgiving (TG), and Brown (BR) Ridges.

patible with models in which the velocity is controlled solely by the elastic and anelastic effects of changing temperature [*Yang et al.*, 2007]. A similar velocity structure has been reported by *Gu et al.* [2005], based on regional Rayleigh wave dispersion along the East Pacific Rise, although in their models, the minimum velocity is somewhat lower and the change in positive velocity gradient at the base of the LVZ occurs at 100 to 110 km instead of ~125 km. The dehydration boundary at 60–70 km may also be responsible for the Gutenberg discontinuity in the oceanic mantle identified in previous studies [e.g., *Revenaugh and Jordan*, 1991; *Gaherty et al.*, 1999]. The onset of decompression melting at 110–125 km and the drying out at 60–70 km are consistent with experimental studies that consider the effects of water in the asthenosphere [*Hirth and Kohlstedt*, 1996].

[37] Seismic anisotropy is well resolved by Rayleigh waves for all periods. The vertical sensitivity provided by the dispersion of Rayleigh waves can also help constrain vertical resolution of anisotropy observed in shear wave splitting methods where vertical resolution is poor due to vertically incident raypaths. The decrease in azimuthal anisotropy with increasing period (Figure 9) indicates that the intrinsic anisotropy decreases with depth, but the persistence of relatively strong anisotropy to at least 60 s period requires intrinsic anisotropy to continue throughout both the lithosphere and the underlying low-velocity zone. Uniform anisotropy of 3.9% over a 50-km-thick lithospheric layer would predict a maximum delay time of about 0.5 s for shear wave splitting. Shear wave splitting measurements from stations in the GLIMPSE experiment, however, indicate much larger splitting times of 1.1 to 2.2 s [*Harmon et al.*, 2004] with fast directions that are consistent with Rayleigh waves and the absolute plate motion of the Pacific Plate. Similarly, shear wave splitting results from the MELT experiment conducted about 100 km south of the GLIMPSE area (Figure 1) also indicate large splitting times of 1.5–2.0 s for the Pacific Plate [*Wolfe and Solomon*, 1998]. These large splitting times also require anisotropy to extend throughout at least the lithosphere and the sublithospheric low-velocity zone, consistent with evidence for upper mantle anisotropy from other studies in the Pacific [e.g., *Montagner*, 2002]. In addition, the change in the direction of anisotropy at long periods for both 2θ and 4θ anisotropic terms (Figure 9b) may indicate a change in azimuth from WNW in the lithospheric plate to EW in the asthenospheric low-velocity zone or deeper although the azimuthal coverage at long periods is poor.

8. The Formation of Intraplate Volcanic Chains in the South Pacific

[38] The four models for formation of intraplate volcanic ridges and gravity lineations summarized in Figure 2 make qualitatively different predictions for the underlying mantle structure. The exact quantitative predictions of the models are less clear, as the seismic velocity anomalies will depend on the predicted melt distribution, shape of melt pockets, water content, frequency dependence of attenuation, temperature dependence of viscosity, and many other somewhat poorly constrained factors. Similarly, the velocity anomalies are imperfectly known, due to inevitable limitations in resolution, so the exact results depend somewhat on starting model, choice of damping or smoothing parameters, unresolved variations in seismic anisotropy, and so on. Nevertheless, there are robust features persistent in all the velocity

models (Figure 8) that provide a clear basis for distinguishing between the classes of tectonic models.

[39] The primary observation is the presence of pronounced low-velocity anomalies in the 10- to 70-km-depth range beneath the volcanic ridges. This thinning or diminution of the high-velocity lid, or lithosphere, is inconsistent with the thermoelastic bending and boudinage models (Figures 2b and 2c). The thermoelastic model involves no alteration of the lithospheric structure. The boudinage model does involve thinning through stretching of the lithosphere, but there are strong constraints on the amount of stretching allowed [*Gans et al.*, 2003] and there is no geomorphological evidence on the seafloor for extension [*Forsyth et al.*, 2006]. Residual bathymetric highs are also present beneath the seamount chains after loading from seamount topography is removed [*Harmon et al.*, 2006b], which is not consistent with the bending and boudinage models that predict downward displacement of the seafloor [*Winterer and Sandwell*, 1987; *Gans et al.*, 2003]. Nevertheless, if we hypothesize that there is locally 20% extension and thinning of the lithosphere in the vicinity of the ridges and assume that the velocity structure above 70 km is stretched by the same amount, filling in below the high-velocity lid with the minimum shear velocity of 3.95 km/s, then the reduction in average velocity in this depth range would be less than 2%, far smaller than the 5–6% anomalies we observe. In addition, both the thermoelastic bending and boudinage models appeal to the tapping of ambient melt in the oceanic asthenosphere through cracks to form the volcanic ridges. Preferential removal of melt should produce high seismic velocities rather than low velocities in the LVZ [e.g., *Karato and Jung*, 1998]. Considering the cross-sectional area of the Sojourn Ridge, which is ~1.5 km high and 10 km wide, melt extraction would require removal of melt from a cross-sectional area of 750 km^2 of mantle for 1% melt concentration or twice that area for a 0.5% concentration. *Hammond and Humphreys* [2006b], for example, estimate a change in V_s of at least 7.9% partial melt in peridotite. This high-velocity anomaly should certainly be detectable within the resolution limits of this study. Instead, we observe anomalously low velocities.

[40] The small-scale convection model suggests that negatively buoyant instabilities in the lower lithosphere develop as the plate cools and are organized into convective rolls aligned with plate motion by shear in the asthenosphere [*Richter and Parsons*, 1975; *Haxby and Weissel*, 1986]. While the low-velocity anomalies observed beneath seamounts in the GLIMPSE area are consistent with this model, the strongest low-velocity anomalies are observed at the youngest ages nearest the EPR (for example, beneath the Brown Ridge in Figures 8 and 12 and the eastern end of Hotu Matua). Low Bouguer gravity anomalies in this region in the vicinity of the seamount lineations extend continuously almost to the rise axis [*Harmon et al.*, 2006b] as does the formation of small seamounts [*White et al.*, 2007]. Numerical and laboratory studies suggest that convective instabilities can form within lithospheric ages as young as 5 Ma [*Buck and Parmentier*, 1986; *Zaranek and Parmentier*, 2004] if mantle viscosities are sufficiently small, ~10^{17} Pa·s. Convective rolls are not expected to form beneath lithosphere less than ~5 Ma, and thus these models do not explain the anomalies in very young seafloor. Small-scale convection at such young ages is not predicted unless the convective roll hypothesis is modified to include the effects of eastward return flow in the upper mantle to the rise axis beneath the westward-traveling Pacific Plate. In this case, lithospheric instabilities that develop off axis beneath lithosphere older than 5 or 10 Ma may be carried back to the EPR by return flow gradients and allow melting, low seismic velocities, and low-gravity anomalies at very young ages. Further geodynamic studies are required to investigate the stability of convective rolls in the presence of plate motion and mantle return flow gradients. Finally, anomalous enrichment of basalts in the seamounts and along the EPR where the seamount chains intersect the spreading center [*Mahoney et al.*, 1994; *Janney et al.*, 2000; *Donnelly et al.*, 2003] is not predicted by the convective roll model unless convection is triggered by compositional anomalies in the asthenosphere instead of inherent lithospheric instability.

[41] The viscous fingering model advocates transport of volatile-rich, anomalously warm material from the Pacific superswell region eastward to the East Pacific Rise axis. The asymmetry in plate subsidence [*Scheirer et al.*, 1998], seismic velocities [*Forsyth et al.*, 1998; *Toomey et al.*, 1998], and anisotropy [*Wolfe and Solomon*, 1998] observed in the MELT experiment southeast of this study is consistent with the idea of asthenospheric transport of anomalously warm mantle from the west [*MELT Seismic Team*, 1998; *Toomey et al.*, 2002; *Conder et al.*, 2002]. If the wavelength of fingering instabilities can predict the ~200-km spacing between the Sojourn, the Hotu Matua, and the Pukapuka Ridges, then the low seismic velocities observed in the GLIMPSE data may be consistent with this model. The sharp positive velocity gradient at the base of the LVZ (Figure 11) supports this model indicating a distinct base below the oceanic asthenosphere to allow fingering instabilities to develop as "channel-like" flow beneath the lithosphere.

[42] This return flow model predicts that pressure release melting may begin due to transport beneath progressively younger and thinner lithosphere of the Pacific Plate. Enrichment in basaltic samples is observed to systematically decrease from west to east for the Sojourn Ridge [*Donnelly et al.*, 2003] as well as the Pukapuka Ridge [*Mahoney et al.*, 1994], consistent with the idea of mantle flow to the spreading ridge from an off-axis plume source. Anomalous mantle flow from the superswell to the spreading ridge beneath this region of the Pacific Plate is also indicated by global circulation [*Forte and Perry*, 2000; *Gaboret et al.*, 2003] and geoid models [*Morgan et al.*, 1995]. The presence of seismic anisotropy in the oceanic asthenosphere suggested by the Rayleigh wave anisotropy and shear wave splitting studies mentioned above is consistent with geodynamic models that invoke asthenospheric flow. Unfortunately, because many OBS's did not contribute data, the lateral resolution of the Rayleigh wave azimuthal anisotropy and the distribution of shear wave splitting measurements for the GLIMPSE experiment were not sufficient to image detailed flow fields that might distinguish convective rolls from unidirectional flow aligned with plate motion.

9. Summary

[43] We present Rayleigh wave phase and shear wave velocity data from the GLIMPSE seismic experiment which

focuses on intraplate seamount chains west of the EPR between 10° and 14°S. Anomalously low phase velocities are observed below the Sojourn Ridge and Hotu Matua seamount complex at periods up to at least 67 s. High velocities are required between the ridges. Sufficient long-period data are available to resolve the shape of the LVZ below the lithosphere. There is a strongly negative shear wave velocity gradient beginning at about 25 km depth leading to a minimum shear velocity of 3.95 km/s at 70 km. We associate the negative velocity gradient with the base of the lithosphere averaged over the study area at 40 ± 15 km depth. The minimum velocity at 70 km is underlain by a sharp positive velocity gradient extending to ~125 km. We suggest that the onset of decompression melting causes the change in shear velocity gradient at ~125 km. Dehydration associated with increased melting and melt removal may be responsible for the reversal in gradient at 70 km.

[44] Azimuthal anisotropy is well resolved from zero at all periods and gradually decreases from a maximum of 3.9% peak-to-peak amplitude with increasing period. The fast azimuth is constant at north of 77°W, parallel to the Pacific Plate motion and the fast direction for shear wave splitting. Anisotropy must extend throughout the lithosphere and the LVZ. We take advantage of the ideal azimuthal distribution of seismic events in this study to test for the importance of the 4θ terms in approximations for azimuthal anisotropy [*Smith and Dahlen*, 1973]. Our results indicate that contribution from the 4θ terms are small but are significantly different from zero for periods up to 60 s, but neglecting these terms introduces little bias in estimates of 2θ terms or lateral variations in velocity.

[45] Anomalously low velocities observed beneath the volcanic ridges and high velocities observed between the chains are consistent with active geodynamic models for seamount formation such as convective rolls or viscous fingering instabilities. Our results do not fit predictions of passive tectonic models such as lithospheric cracking or plate bending, which invoke the tapping of preexisting, widespread melt in the asthenosphere. The convective roll hypothesis must be modified, however, to invoke some mechanism such as mantle return flow currents that sweep instabilities which form at older ages, back to the EPR, where low seismic velocities, low Bouguer gravity anomalies, and small seamounts are observed. Viscous fingering at asthenospheric depths could introduce compositional anomalies that would vary in enrichment from west to east and continue all the way to the EPR spreading center. In addition, anomalous melting of these compositional heterogeneities could induce small-scale convection that would amplify their effect.

[46] **Acknowledgments.** The associate editor and Jean-Paul Montagner provided critical reviews that strengthened this paper. This work benefited in its entirety from the newly established U.S. National OBS Instrument Pool. We thank the captains and crews of the R/V Melville for their dedication and proficiency. This research was supported by the National Science Foundation under grant OCE-9911729.

References

Brune, J., and J. Dorman (1963), Seismic waves and earth structure in the Canadian Shield, *Bull. Seismol. Soc. Am.*, *53*, 167–209.

Buck, W. R., and E. M. Parmentier (1986), Convection beneath young oceanic lithosphere: Implications for thermal structure and gravity, *J. Geophys. Res.*, *91*, 1961–1974.

Cazenave, A., S. Houry, B. Lago, and K. Dominh (1992), Geosat-derived geoid anomalies at medium wavelength, *J. Geophys. Res.*, *97*, 7081–7096.

Collins, J. A., F. L. Vernon, J. A. Orcutt, and R. A. Stephen (2003), Upper mantle structure beneath the Hawaii swell: Constraints from the ocean seismic network pilot experiment, *Geophys. Res. Lett.*, *29*(11), 1522, doi:10.1029/2001GL013302.

Conder, J. A., D. W. Forsyth, and E. M. Parmentier (2002), Asthenospheric flow and asymmetry of the East Pacific Rise, MELT Area, *J. Geophys. Res.*, *107*(B12), 2344, doi:10.1029/2001JB000807.

Davaille, A., and C. Jaupart (1994), Onset of thermal convection in fluids with temperature-dependent viscosity: Application to the oceanic mantle, *J. Geophys. Res.*, *99*, 19,853–19,866.

Donnelly, K. E., C. H. Langmuir, and S. L. Goldstein (2003), Geochemical constraints on melting process in the GLIMPSE region, *EOS Trans. AGU*, *84*(46), Fall Meet. Suppl., Abstract V21B-05.

Dunbar, J. A., and D. T. Sandwell (1988), A boudinage model for cross-grain lineations, *EOS Trans. AGU*, *69*(44), 1429, Meet. Suppl., Abstract.

Evans, R. L., G. Hirth, K. Baba, D. Forsyth, A. Chave, and R. Mackie (2005), Geophysical evidence from the MELT area for compositional controls on oceanic plates, *Nature*, *437*, 249–252.

Faul, U. H., and I. Jackson (2005), The seismological signature of temperature and grain size variations in the upper mantle, *Earth Planet. Sci. Lett.*, *234*, 119–134.

Forsyth, D. W. (1975), The early structural evolution and anisotropy of the oceanic upper mantle, *Geophys. J. R. Astron. Soc.*, *43*, 103–162.

Forsyth, D. W., and A. Li (2005), Array-analysis of two-dimensional variations in surface wave velocity and azimuthal anisotropy in the presence of multipathing interference, in *Seismic Earth Array Analysis of Broadband Seismograms*, edited by A. Levander and G. Nolet, vol. 157, 81–97, AGU Geophysical Monograph, doi:10.1029/1566GM06.

Forsyth, D. W., S. C. Webb, L. M. Dorman, and Y. Shen (1998), Phase velocities of Rayleigh waves in the MELT experiment on the East Pacific Rise, *Science*, *280*, 1235–1237.

Forsyth, D. W., N. Harmon, D. S. Scheirer, and R. A. Dunn (2006), The distribution of recent volcanism and the morphology of seamounts and ridges in the GLIMPSE study area: Implications for the lithospheric cracking hypothesis for the origin of intraplate, non-hotspot volcanic chains, *J. Geophys. Res.*, *111*, B11407, doi:10.1029/2005JB004075.

Forte, A. M., and H. K. C. Perry (2000), Geodynamic evidence for a chemically depleted continental tectosphere, *Science*, *290*, 1940–1944.

Gaboret, C., A. M. Forte, and J. P. Montagner (2003), The unique dynamics of the Pacific hemisphere mantle and its signature on seismic anisotropy, *Earth Planet. Sci. Lett.*, *208*, 219–233.

Gaherty, J., M. Kato, and T. H. Jordan (1999), Seismological structure of the upper mantle: A regional comparison of seismic layering, *Phys. Earth Planet. Inter.*, *110*, 21–41.

Gans, K. D., D. S. Wilson, and K. C. Macdonald (2003), Pacific plate gravity lineaments: Diffuse extension or thermal contraction?, *Geochem. Geophys. Geosyst.*, *4*(9), 1074, doi:10.1029/2002GC000465.

Goff, J. A., and J. R. Cochran (1996), The Bauer scarp ridge jump: A complex tectonic sequence revealed in satellite altimetry, *Earth Planet. Sci. Lett.*, *141*, 21–33.

Goodwillie, A. M., and B. Parsons (1992), Placing bounds on lithospheric deformation in the central Pacific Ocean, *Earth Planet. Sci. Lett.*, *111*, 123–139.

Gu, Y. J., S. C. Webb, A. L. Lam, and J. B. Gaherty (2005), Upper mantle structure beneath the eastern Pacific ocean ridges, *J. Geophys. Res.*, *110*, B06305, doi:10.1029/2004JB003381.

Hammond, W. C., and E. D. Humphreys (2000a), Upper mantle seismic wave attenuation: Effects of realistic partial melt distribution, *J. Geophys. Res.*, *105*, 10,987–11,000.

Hammond, W. C., and E. D. Humphreys (2000b), Upper mantle seismic wave velocity: Effects of realistic partial melt geometries, *J. Geophys. Res.*, *105*, 10,975–10,986.

Harmon, N., D. W. Forsyth, and K. M. Fischer (2004), Variations in shear-wave splitting in young Pacific seafloor, *Geophys. Res. Lett.*, *31*, L15609, doi:10.1029/2004GL020495.

Harmon, N., D. W. Forsyth, R. Lamm, and S. C. Webb (2006a), P and S wave delays beneath intraplate volcanic ridges and gravity lineations near the East Pacific Rise, *J. Geophys. Res.*, *112*, B03309, doi:10.1029/2005JB004392.

Harmon, N., D. W. Forsyth, and D. S. Scheirer (2006b), Analysis of gravity and topography in the GLIMPSE region: Isostatic compensation and uplift of the Sojourn and Hotu Matua ridge systems, *J. Geophys. Res.*, B11406, doi:10.1029/2005JB004071.

Haxby, W. F., and J. K. Weissel (1986), Evidence for small-scale mantle convection from Seasat altimeter data, *J. Geophys. Res.*, *91*, 3507–3520.

Hill, S. (1952), Channelling in packed columns, *Chem. Eng. Sci.*, *1*, 247–253.

Hirth, G., and D. L. Kohlstedt (1996), Water in the oceanic upper mantle: Implications for rheology, melt extraction and evolution of the lithosphere, *Earth Planet. Sci. Lett.*, *144*, 91–108.

Holmes, C., S. Webb, and D. W. Forsyth (2007), Crustal structure beneath gravity lineations in the GLIMPSE study area from seismic refraction data, *J. Geophys. Res.*, doi:10.1029/2006JB004685, in press.

Jackson, I., U. H. Faul, J. D. Fitz Gerald, and B. H. Tan (2004), Shear wave attenuation and dispersion in melt-bearing olivine polycrystals: 1. Specimen fabrication and mechanical testing, *J. Geophys. Res.*, *109*, B06201, doi:10.1029/2003JB002406.

Janney, P. E., J. D. Macdougall, J. H. Natland, and M. A. Lynch (2000), Geochemical evidence from the Pukapuka volcanic ridge system for a shallow enriched mantle domain beneath the South Pacific superswell, *Earth Planet. Sci. Lett.*, *181*, 47–60.

Jha, J., E. M. Parmentier, and D. W. Sparks (1997), Buoyant mantle upwelling and crustal production at oceanic spreading centers: On-axis segmentation and off-axis melting, *J. Geophys. Res.*, *102*, 11,979–11,989.

Karato, S., and H. Jung (1998), Water, partial melting and the origin of the seismic low velocity and high attenuation zone in the upper mantle, *Earth Planet. Sci. Lett.*, *157*, 193–207.

Llenos, A. L., D. W. Forsyth, and S. C. Webb (2003), Microearthquakes near Matua seamount, GLIMPSE study area, *EOS Trans. AGU*, *84*(46), Fall Meet. Suppl., Abstract V12B-0583.

Li, A., D. W. Forsyth, and K. M. Fischer (2002), Evidence for shallow isostatic compensation of the southern Rocky Mountains and Rayleigh wave tomography, *Geology*, *30*, 683–686.

Li, A., D. W. Forsyth, and K. M. Fischer (2003), Shear velocity structure and azimuthal anisotropy beneath eastern North America from Rayleigh wave inversion, *J. Geophys. Res.*, *108*(B8), 2362, doi:10.1029/2002JB002259.

Lonsdale, P. G. (1988), Segmentation of the Pacific-Nazca spreading center, 1°N–20°S, *J. Geophys. Res.*, *93*, 2813–2838.

Mahoney, J. J., J. M. Sinton, M. D. Kurz, J. D. Macdougall, K. J. Spencer, and G. W. Lugmair (1994), Isotope and trace element characteristics of a super-fast spreading ridge: East Pacific Rise, 13–23°, *Earth Planet. Sci. Lett.*, *121*, 173–193.

McNutt, M. K. (1998), Superswells, *Rev. Geophys.*, *36*, 211–244.

Melt Seismic Team (1998), Imaging the deep seismic structure beneath a mid-ocean ridge: The MELT Experiment, *Science*, *280*, 1215–1218.

Montagner, J. P. (2002), Upper mantle low anisotropy channels below the Pacific, *Earth Planet. Sci. Lett.*, *202*, 263–274.

Montagner, J. P., and H. C. Nataf (1986), A simple method for inverting the azimuthal anisotropy of surface waves, *J. Geophys. Res.*, *91*, 511–520.

Montelli, R., G. Nolet, F. A. Dahlen, G. Masters, E. R. Engdahl, and S. H. Hung (2004), Finite-frequency tomography reveals a variety of plumes in the mantle, *Science*, *303*(5656), 338–343.

Morgan, J. P., W. J. Morgan, Y. Zhang, and W. H. F. Smith (1995), Observational hints for a plume-fed, suboceanic asthenosphere and its role in mantle convection, *J. Geophys. Res.*, *100*, 12,753–12,767.

Nishimura, C. E., and D. W. Forsyth (1988), Rayleigh wave phase velocities in the Pacific with implications for azimuthal anisotropy and lateral heterogeneities, *Geophys. J.*, *94*, 479–501.

Nishimura, C. E., and D. W. Forsyth (1989), The anisotropic structure of the upper mantle in the Pacific, *Geophys. J.*, *96*, 203–209.

Revenaugh, J., and T. H. Jordan (1991), Mantle layering from ScS reverberations: 3. The upper mantle, *J. Geophys. Res.*, *96*, 19,781–19,810.

Richardson, W. P., E. A. Okal, and S. V. Lee (2000), Rayleigh-wave tomography of the Ontong-Java Plateau, *Phys. Earth Planet. Inter.*, *118*, 29–51.

Richter, F. M., and B. Parsons (1975), On the interaction of two scales of convection in the mantle, *J. Geophys. Res.*, *80*, 2529–2541.

Saffman, P. G., and G. T. Taylor (1958), The penetration of a fluid into a porous medium or Hele-Shaw cell containing a more viscous liquid, *Proc. R. Soc. Ser. A*, *245*, 312–329.

Saito, M. (1988), DISPER80: A subroutine package for the calculation of seismic normal-mode solutions, in *Seismological Algorithms*, edited by D. J. Doornbos, 293–319, Elsevier, New York.

Saltzer, R. (2002), Upper mantle structure of the Kaapvaal craton from surface wave analysis—A second look, *Geophys. Res. Lett.*, *29*(6), 1093, doi:10.1029/2001GL013702.

Sandwell, D. T., and Y. Fialko (2004), Warping and cracking of the Pacific plate by thermal contraction, *J. Geophys. Res.*, *109*, B10401, doi:10.1029/2004JB003091.

Sandwell, D. T., E. L. Winterer, J. Mammerickx, R. A. Duncan, M. A. Lynch, D. A. Levitt, and C. L. Johnson (1995), Evidence for diffuse extension of the Pacific plate from Pukapuka ridges and cross-grain gravity lineations, *J. Geophys. Res.*, *100*, 15,087–15,099.

Scheirer, D. S., D. W. Forsyth, M. H. Cormier, and K. C. Macdonald (1998), Shipboard geophysical indications of asymmetry and melt production beneath the East Pacific Rise near the MELT experiment, *Science*, *280*, 1221–1223.

Schilling, J. G., D. Fontignie, J. Blichert-Toft, R. Kingsley, and U. Tomza (2003), Pb-Jf-Nd-Sr isotope variations along the Galápagos spreading center (101°–83°): Constraints on the dispersal of the Galapagos mantle plume, *Geochem. Geophys. Geosyst.*, *4*(10), 8512, doi:10.1029/2002GC000495.

Schmeling, H. (2000), Partial melting and melt segregation in a convecting mantle, in *Physics and Chemistry of Partially Molten Rocks*, edited by N. Bagdassarov, D. Laporte, and A. B. Thompson, Springer, New York.

Smith, M. L., and F. A. Dahlen (1973), The azimuthal dependence of Love and Rayleigh wave propagation in a slightly anisotropic medium, *J. Geophys. Res.*, *78*, 3321–3333.

Stixrude, L., and C. Lithgow-Bertelloni (2005), Mineralogy and elasticity of the oceanic upper mantle, origin of the low-velocity zone, *J. Geophys. Res.*, *110*, B03204, doi:10.1029/2004JB002965.

Tarantola, A., and B. Valette (1982), Generalized non-linear inverse problems solved using the least-squares criterion, *Rev. Geophys. Space Phys.*, *20*, 219–232.

Toomey, D. R., W. S. D. Wilcock, S. C. Solomon, W. C. Hammond, and J. A. Orcutt (1998), Mantle seismic structure beneath the MELT region of the East Pacific Rise from P and S wave tomography, *Science*, *280*, 1224–1226.

Toomey, D. R., W. S. D. Wilcock, J. A. Conder, D. W. Forsyth, J. Blundy, E. M. Parmentier, and W. C. Hammond (2002), Asymmetric mantle dynamics in the MELT region of the East Pacific Rise, *Earth Planet. Sci. Lett.*, *200*, 287–295.

Webb, S. C. W., T. K. Deaton, and J. C. Lemire (2001), A broadband ocean-bottom seismometer system based on a 1-Hz natural period geophone, *Bull. Seismol. Soc. Am.*, *91*, 304–312.

Weeraratne, D. S., D. W. Forsyth, and K. M. Fischer (2003a), Evidence for an upper mantle plume beneath the Tanzanian craton from Rayleigh wave tomography, *J. Geophys. Res.*, *108*(B9), 2427, doi:10.1029/2002JB002273.

Weeraratne, D. S., E. M. Parmentier, and D. W. Forsyth (2003b), Viscous fingering instabilities in miscible fluids and the oceanic asthenosphere, *EOS Trans. AGU*, *84*(46), Fall Meet. Suppl., Abstract V21B-03, Invited.

White, D. M., S. Umino, and H. Kmagai (2007), Transition from seamount chain to submarine volcanic ridge at the East Pacific Rise, *Geology*, in press.

Winterer, E. L., and D. T. Sandwell (1987), Evidence from en-echelon cross-grain ridges for tensional cracks in the Pacific plate, *Nature*, *329*, 534–537.

Wolfe, C. J., and S. C. Solomon (1998), Shear-wave splitting and implications for mantle flow beneath the MELT region of the East Pacific Rise, *Science*, *280*, 1230–1232.

Yang, Y., and D. W. Forsyth (2006a), Regional tomographic inversion of amplitude and phase of Rayleigh waves with 2-D sensitivity kernels, *Geophys. J. Int.*, *166*, 1148–1160.

Yang, Y., and D. W. Forsyth (2006b), Rayleigh wave phase velocities, small-scale convection and azimuthal anisotropy beneath southern California, *J. Geophys. Res.*, *111*, B07306, doi:10.1029/2005JB004180.

Yang, Y., D. W. Forsyth, and D. S. Weeraratne (2007), Seismic attenuation near the East Pacific Rise and the origin of the low-velocity zone, *Earth Planet. Sci. Lett.*, doi:10.1016/j.epsl.2007.03.040, in press.

Zaranek, S. E., and E. M. Parmentier (2004), Convective cooling of an initially stably stratified fluid with temperature-dependent viscosity: Implications for the role of solid-state convection in planetary evolution, *J. Geophys. Res.*, *109*, B03409, doi:10.1029/2003JB002462.

Zhou, Y., A. Dahlen, and G. Nolet (2004), Three-dimensional sensitivity kernels for surface-wave observables, *Geophys. J. Int.*, *158*, 142–168.

D. W. Forsyth, D. S. Weeraratne, and Y. Yang, Department of Geological Sciences, Brown University, 324 Brook St., Providence, RI 02912-9019, USA. (donald_forsyth@brown.edu; weeraratne@dtm.ciw.edu; dsw@csun.edu; yingjie@ciei.colorado.edu)

S. C. Webb, Lamont-Doherty Earth Observatory, Columbia University, P.O. Box 1000, Palisades, NY 10964, USA. (scw@ldeo.columbia.edu)